

Atomically clean free-standing two-dimensional materials through heating in ultra-high vacuum

Philipp Irschik^{1,2,*}, David Lamprecht^{1,3}, Shrirang Chokappa^{1,2}, Clemens Mangler¹, Carsten Speckmann¹, Thuy An Bui^{1,2}, Manuel Längle¹, Lado Filipovic³, Jani Kotakoski^{1,*}

¹University of Vienna, Faculty of Physics, Boltzmanngasse 5, 1090 Vienna, Austria

²University of Vienna, Vienna Doctoral School in Physics, Boltzmanngasse 5, 1090 Vienna, Austria

³Institute for Microelectronics, TU Wien, Gußhausstraße 27-29/E360, 1040 Vienna, Austria

*Email: philipp.irschik@univie.ac.at, jani.kotakoski@univie.ac.at

August 28, 2025

Abstract

Surface contamination not only influences but in some cases even dominates the measured properties of two-dimensional materials. Although different cleaning methods are often used for contamination removal, commonly used spectroscopic cleanliness assessment methods can leave the level of achieved cleanliness ambiguous. Despite two decades of research on 2D materials, the true cleanliness of the used samples is often left open to interpretation. In this work, free-standing monolayer graphene and hexagonal boron nitride are annealed at different temperatures in a custom-built ultra-high vacuum heating chamber, connected to a scanning transmission electron microscope via a vacuum transfer line, enabling atomically resolved cleanliness characterization as a function of annealing temperature, while eliminating the introduction of airborne contamination during sample transport. While annealing at 200 °C already reduces contamination significantly, it is not until 400 °C or higher, where over 90% of the free-standing monolayer areas are atomically clean. At this point, further contamination removal is mainly limited by defects in the material and metal contamination introduced during the sample transfer or growth. The achieved large, atomically clean areas can then be used for further nanoscale engineering steps or device processing, facilitating interaction with the material rather than contamination.

Introduction

Two-dimensional (2D) materials, such as monolayer graphene and hexagonal boron nitride (h-BN) possess a much larger surface-to-volume ratio compared to bulk materials, leading to an amplified effect of the often undesired surface contamination, which can result in the degradation of a variety of the materials' intrinsic properties, including their charge carrier mobility^[1–3], wettability^[4], and thermal conductivity^[5,6]. Additionally, the extent of its impact can vary between samples or even within different areas of the same specimen due to the lack of control over it, hindering reproducibility in device operations^[7]. Furthermore, even a thin film of adsorbed contaminants can obstruct the underlying material, with clean areas often being only a few to tens of nanometers in size^[8]. This can be detrimental to contrast-based imaging techniques, such as (scanning) transmission electron microscopy, particularly for atomically thin free-standing specimens, where the signal of interest comes only from one to a few layers of atoms, and clean areas larger than a few nanometers are often desired^[9]. These are necessary, as the observed properties may actually stem from interactions with contamination^[10–12] rather than the material itself^[13,14], and could lead to misinterpretation and misreporting of the properties of the studied materials.

Even though in-situ methods for sample preparation of 2D materials have been developed^[15], it is still common to use ex-situ procedures, such as mechanical exfoliation, molecular beam epitaxy, or chemical vapor deposition (CVD), where the prepared samples are exposed to ambient conditions, either during or after the synthesis process^[16–18], resulting in exposure to airborne hydrocarbon contamination, silicon, water vapor, and molecular oxygen already after a few minutes^[4,19–22]. Also, transferring the materials onto other surfaces is typically needed for further device fabrication or applications, a process that often involves direct contact with polymers like poly(methyl methacrylate) (PMMA)^[23,24]. While organic solvents like acetone and chloroform^[25] can be used to dissolve PMMA after the transfer, they often fail to remove it completely, and can thus leave a thin film of polymer adsorbed on the surfaces^[26–28], obstructing the underlying materials, and degrading their properties^[3].

This ubiquitous presence of surface contamination has incentivized the development of various post-preparation cleaning methods. While specialized cleaning techniques like cleaning in activated carbon^[19,29], electrolytic cleaning^[30], or annealing with the aid of metal catalysts^[31,32] have been explored, they are not suitable for all applications and often require specialized device fabrication. Thus, methods such as mechanical cleaning, plasma cleaning, laser cleaning, current-induced annealing, and thermal annealing are still often used^[33].

While mechanical cleaning methods can produce atomically clean areas by breaking the van der Waals bonds between the contamination and the underlying material using tips commonly used in atomic force microscopy (AFM)^[22,34], this is an inherently slow process and thus does not scale well to larger areas. Plasma cleaning can be effective in etching surface-bound polymer contamination^[28], however, a successful etching process relies on carefully chosen parameters for the plasma energy and density, as well as treatment duration, to not damage the underlying material in the process^[35,36]. Cleaning techniques using laser ablation can also effectively remove contamination, but are limited to the laser spot size, restricting their application on the larger scale^[37,38], and methods like current-induced annealing are limited to electrically conductive materials and require electrode attachment^[39–41]. Therefore, thermal solutions for sample cleaning are often used due to their rather simple installation and ease of use. Many setups allow annealing in controlled ambient environments, such as inert, reducing, and oxidizing atmospheres, as well as vacuum, the selection of which can have a drastic effect not only on the cleaning process but also on the integrity of the 2D material, with electrical doping^[42,43], defect formation^[44,45], induced strain^[46,47], and graphitization of carbonaceous contamination^[48] being common side effects of thermal annealing processes.

For graphene, even at temperatures as high as 500 °C, inert atmospheres have been reported to be ineffective at completely removing PMMA residue^[49], and can turn it into covalently bonded amorphous carbon, which makes it difficult to remove^[30,50]. Reducing atmospheres can facilitate depolymerization of polymer residue when annealed at 400 °C or higher^[42], with H₂ and Ar/H₂ being particularly effective in removing residual conjugated carbon systems by transforming

them into light hydrocarbons^[51]. However, this tends to induce rehybridization of graphene from sp^2 to sp^3 , resulting in amorphous carbon^[44,46], as well as strong p -type doping^[43]. Annealing in oxidizing atmospheres, while being effective in decomposing amorphous carbon contamination^[52], can cause the formation of cracks in graphene at temperatures as low as 200 °C^[44], and still fails to remove all contaminants, even at 500 °C^[38]. Also, it has been found that the oxidative strength of the atmosphere has a strong effect on the etching characteristics, as NO₂ seems to completely etch graphene away when annealed above 500 °C, while CO₂ preserves it^[45]. Thermal annealing in vacuum, while reported to be unable to remove contamination completely^[2,27,49,53], seems to introduce the least amount of lattice defects compared to other thermal annealing treatments due to the lack of reactive species in the annealing atmosphere^[25]. In addition, the amount of induced hole doping and strain is reported to be minimal^[43,47], while providing satisfactory cleaning results^[38,49]. The purity of the vacuum must be kept in mind though, as annealing under better vacuum conditions reportedly yields cleaner specimens^[50]. Pressure values in the 10⁻³ mbar range have been shown to be ineffective at reliably cleaning graphene surfaces^[49], compared to annealing in high vacuum^[25] or ultra-high vacuum (UHV)^[2,27,47,53], where large atomically clean surfaces have been achieved^[38], making UHV annealing a suitable candidate for contamination removal without harming the integrity of the underlying material.

Despite this established understanding of polymer degradation as well as hydrocarbon species desorption^[54,55] on graphene surfaces, there is still a lack of reporting on the cleaning of monolayer h-BN despite its various projected applications, such as being a dielectric for nanoelectronic devices^[56-60], and for quantum information and sensor technology due to its quantum light emission across a wide spectral range^[61-65]. Particularly, the latter relies on atomically clean surfaces to reliably conduct atomically-precise defect creation^[66-68] or carbon doping^[69-71] to create active sites for single photon emission. While surface contamination reduction via thermal annealing of h-BN has previously been utilized, including annealing in oxidizing environments^[72-75], and UHV^[76,77], the reports either lack information on the structure and abundance of contaminants as a function of annealing temperature, or do not employ atomically resolved

characterization techniques, leaving open the possibility of a thin layer of contaminants remaining on the surface.

In this work, we investigate the effect of thermal annealing in UHV on CVD-grown and wet-transfer-assisted free-standing monolayer graphene and h-BN, using a custom-built UHV heating chamber that is connected to a scanning transmission electron microscope through a vacuum transfer line. This ensures that the cleaning effect can be directly characterized without introducing airborne contaminants in the process. Contrary to commonly used spectroscopic assessment methods with limited spatial resolutions, including Raman spectroscopy^[30,43], X-ray photoelectron spectroscopy^[2,35,42,49], and time-of-flight secondary ion mass spectrometry^[27,47], we employ atomically resolved scanning transmission electron microscopy (STEM) to identify the presence of contamination on monolayer graphene and h-BN surfaces as a function of temperature down to the atomic level. Using annular dark field (ADF)-STEM imaging, we can identify the position, shape, and abundance of contamination due to its higher scattering intensity compared to atomically clean free-standing monolayer regions. Using contrast-based image thresholding and segmentation to separate contaminated from clean areas, we determine the relative amount of surface area covered by contamination, a procedure that is carried out for different transfer methods and baking temperatures, correlating the relative clean monolayer area of graphene and h-BN with annealing temperature. This is complemented with electron energy loss spectroscopy (EELS) measurements before and after the annealing steps, giving insight into the composition of the contamination that survives the heating process, which is one of the main limitations for obtaining truly residue-free materials.

Methods

Microscopy and spectroscopy

All STEM measurements were carried out using a Nion UltraSTEM 100, an aberration-corrected scanning transmission electron microscope, operated at an acceleration voltage of 60 kV, with a beam convergence semiangle of 30 mrad and a probe size of approximately 1 Å. The base pressure at the sample stage inside the microscope column was in the low 10^{-9} mbar range or lower at all times. The images were acquired using medium-angle annular dark field (MAADF) and

high-angle annular dark field (HAADF) detectors with collection semiangular ranges of 60-200 mrad and 80-300 mrad, respectively.

EELS measurements were carried out using a Gatan PEELS 666 spectrometer with an Andor iXon 897 electron-multiplying charge coupled device (EMCCD). All EEL spectra were acquired with a total of 512 pixels and an energy dispersion of 0.5 eV/pixel at a collection semiangle of 35 mrad. All original spectra, including their background subtraction, are found in the Supporting Information.

Digital image processing

HAADF-STEM images of graphene and h-BN that were acquired at a nominal field of view (FOV) of $128 \times 128 \text{ nm}^2$ ($1024 \times 1024 \text{ px}$, pixel time $8 \mu\text{s}$) were subsequently subjected to a thresholding-based automated digital image processing algorithm to identify the relative abundance of clean monolayer regions in the frame. The lower thickness and thus lower scattering intensity of clean monolayer regions compared to contamination and multilayer structures in STEM enable contrast-based image thresholding and segmentation, with an example shown in Supplementary Figure S2 (Supporting Information). For graphene samples heated at 450°C , images of entire holes ($1024 \times 1024 \text{ nm}^2$ FOV nominally, $4096 \times 4096 \text{ px}$, pixel time $8 \mu\text{s}$) in the sample support were acquired and thresholded instead, where a circular mask with a diameter of 950 nm was applied to mask the sample support area. We refer to the Supporting Information for a detailed description of the digital image processing steps.

Sample preparation

Graphene— We used commercially available "Easy Transfer" monolayer graphene (Graphenea, Inc.), which is sandwiched between a $100 \mu\text{m}$ thick porous water-releasable polymer support film and a sacrificial PMMA layer. It was cut into small (ca. $3 \times 3 \text{ mm}^2$) squares roughly matching the size of a TEM grid. The graphene/PMMA stack was separated from the polymer support by dipping it into deionized (DI)-water, making it float on the water's surface due to the hydrophobic nature of PMMA. The stack was then fished out with a TEM grid with a Quantifoil amorphous carbon support film

(Quantifoil R 1.2/1.3 Au grid), after which it was left to dry in air on a standard laboratory hot plate at 150 °C for 1 h. It was then placed into a hot acetone (SigmaAldrich, ACS reagent, $\geq 99.5\%$) bath for 1 h to dissolve the majority of the PMMA residue, followed by a wash in isopropyl alcohol (IPA) (SigmaAldrich, ACS reagent, $\geq 99.5\%$) at room temperature for 45 min.

After investigating the sample quality and observing a large amount of metallic residue on all samples transferred this way, both before and after the annealing steps, further graphene samples were prepared via electrochemical delamination^[78] using commercial monolayer graphene on Cu with PMMA coating (Graphenea, Inc.). To delaminate the samples, after cutting them to size as described above, a platinum anode was placed into NaOH (SigmaAldrich, ACS reagent, $\geq 95.0\%$, pellets) aqueous solution (1 M), with the Cu/graphene/PMMA stack on Inox 02 tweezers acting as the cathode. All samples were delaminated at a voltage of 4 V. Afterwards, the delaminated graphene/PMMA stack was washed in DI-water to remove residual NaOH contamination, after which it was fished out with a TEM grid with a Quantifoil holey amorphous carbon membrane (Quantifoil R 1.2/1.3 Au grid), followed by a hot acetone bath for 1 h, with a final wash in IPA for 45 min. One additional sample was transferred onto a holey silicon nitride support film (PELCO, 3 mm diameter, 200 μm silicon support structure, 0.5 \times 0.5 mm window, 200 nm membrane thickness, 1 μm pore size) using the same transferring steps.

Hexagonal boron nitride— After sourcing monolayer h-BN from three different suppliers, we chose monolayer h-BN on copper from SigmaAldrich due to their superior monolayer coverage (Figure S11, Supporting Information), cut into small squares, which was spin-coated with PMMA (ALLRESIST AR-P 642.04, 200K) for 15 s at 500 RPM, followed by 15 s at 1000 RPM, and finally 60 s at 2000 RPM, at a ramp of 100 RPM/s. The Cu/h-BN/PMMA stack was placed on a glass slide, where the PMMA was left to cure on a hot plate at 150 °C for 30 min in air. After the PMMA had hardened, less than 1 mm was cut from all edges of the square to remove PMMA spillover to the other side of the foil. The subsequent delamination and washing steps were analogous to the graphene samples transferred via electrochemical

delamination as described above.

UHV heating chamber

All annealing experiments were carried out in a custom-built UHV heating chamber integrated into the CANVAS system at the University of Vienna^[79], with a base pressure typically around 5×10^{-9} mbar or lower. The samples are annealed via resistive heating of a tungsten filament that is placed out of the line of sight of the samples to avoid locally high temperatures and deposition of material coming off the wire. A more thorough description, including design sketches and used materials, can be found in the Supporting Information.

All samples were inserted at room temperature, after which the tungsten wire power was gradually increased to initiate the heating process, with typical heating rates between 0.1 °C/s and 1 °C/s, depending on the target temperature. The temperature was controlled by regulating the output current of the power supply using a proportional-integral-derivative (PID) control algorithm. Upon reaching the desired temperature, the samples were kept at the setpoint for 3 h, after which the wire power was decreased to zero over five minutes. The samples were then kept in the chamber for about 30 min to passively cool down to temperatures between 150 °C – 250 °C (depending on the baking temperature) before being transferred to the microscope for characterization.

Results and Discussion

We use commercial CVD-grown monolayer graphene and h-BN, which were transferred onto TEM grids using a PMMA-assisted wet transfer process (see Methods). The majority of the PMMA residue was removed from the surface by placing the samples into an acetone bath, followed by a further washing step in IPA. After preparation, the samples were inserted into the CANVAS system at the University of Vienna^[79], which allows transporting the samples between a customized aberration-corrected scanning transmission electron microscope (Nion UltraSTEM 100)^[80], and a custom-built UHV heating chamber without breaking the near-UHV conditions in between. This is integral to assessing the samples' cleanliness since this allows the cleaning effect to be directly characterized without intermediary air exposure.

Upon insertion into the loadlock of the CANVAS system, they were subjected to a routine bake at 160 °C for over 10 h in high vacuum to remove water and reduce the amount of surface contamination to avoid contaminating the UHV system. Using the Nion UltraSTEM 100, all samples were investigated for coverage and cleanliness before the UHV annealing step, after which they were transferred to the UHV heating chamber and annealed at different temperatures for 3 h. After the baking procedure had finished, the samples were immediately returned to the microscope for post-heating characterization to minimize the effect of electron-beam-induced hydrocarbon deposition^[81].

To assess the cleanliness of the samples, both before and after the thermal treatment, up to ten typical holes (1 μm nominal diameter) in the sample support were imaged. The holes were chosen based on average and characteristic features resulting from each heating process. Different holes in the sample support were selected before and after each heating step, as the dissociation and subsequent cross-linking of the hydrocarbon contaminants from prior e-beam exposure interferes with heating-induced contamination removal^[82]. Approximately 20 arbitrarily chosen, non-overlapping areas with nominal FOV of $128 \times 128 \text{ nm}^2$ were captured within each hole, acquiring a total of ca. 150 - 200 frames per temperature and sample. At each new frame position, the electron beam was manually re-focused onto the sample surface to obtain lattice resolution, minimizing out-of-focus features in the contamination at the interface to the material's surface. We note that no electron-beam-induced hydrocarbon deposition was observed during any measurement, and refer to the Supporting Information for a more thorough discussion.

Easy Transfer Graphene

All as-prepared Easy Transfer Graphene samples exhibited a high amount of metallic contamination in the form of nanosized iron and copper clusters in addition to carbonaceous contamination covering practically the entire surface. While atomically clean monolayer regions could be found, they were small in size, typically less than 10 nm in diameter, and accounted for less than 5% of the free-standing regions (Figure 1a, blue dots). Example areas of contaminated and cleaned Easy Transfer Graphene are shown in Figure 1b. Heating to 250 °C did result in some removal of organic residue,

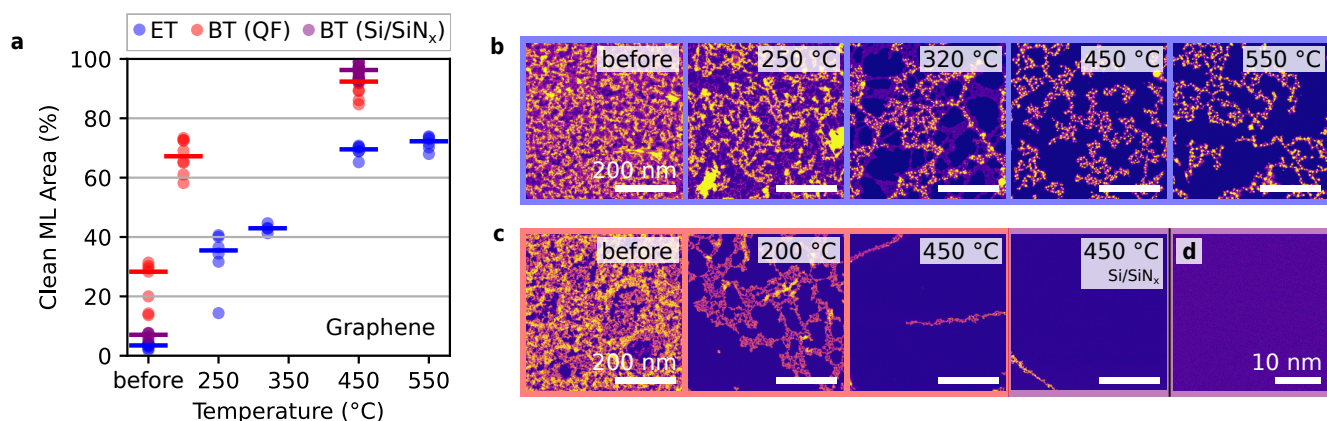


Figure 1: Graphene cleanliness after annealing at different temperatures. a) Relative clean monolayer (ML) area as a function of annealing temperature for Easy Transfer Graphene (ET, blue) on Quantifoil (QF), and graphene transferred via bubbling transfer (BT) on QF (red) and Si/SiN_x (purple). Each dot (up to ten per temperature) represents the relative amount of clean monolayer area in an imaged hole in the sample support. The horizontal bars show the median. b) Cropped MAADF-STEM images of typical regions of free-standing monolayer Easy Transfer Graphene on QF before and after annealing at different temperatures. The darkest contrast is clean graphene, the brighter contrast is contamination. c) Graphene transferred onto QF and Si/SiN_x via electrochemical delamination before and after annealing at different temperatures. d) Averaged MAADF-STEM image (50 frames) of large-area pristine monolayer graphene on Si/SiN_x after heating at 450 °C for 2 h. Scale bars: b,c) 200 nm, d) 10 nm. The non-cropped images of the frames shown in panels b) and c) can be found in Supplementary Figure S7. Contrast has been adjusted to highlight relevant features, and we refer to Supplementary Figure S1 for the false color grading reference.

increasing the average exposed clean area to 35%. The sizes of the now uncovered clean areas remained small (around 20 - 30 nm in diameter), indicating that higher temperatures are needed. Heating to 320 °C uncovered more of the surface area (ca. 40%), however, we identified thin hydrocarbon contamination networks all over the surface with only a marginal increase in the uncovered clean area compared to the 250 °C treatment. While annealing at 450 °C removed the majority of the carbonaceous contamination, resulting in a 70% relative clean monolayer area, with clean regions wider than 200 nm being common, we identified networks of metal clusters embedded in carbon-rich contamination as the primary residual contamination. Raising the annealing temperature to 550 °C did not increase the unveiled clean area, which remained at around 70%. This not only indicates that the achievable cleanliness via UHV annealing is heavily limited by the residual metal contaminants introduced during the sample growth and transfer process, but also that temperatures above 400 °C appear to be sufficient to remove almost all of the carbonaceous contamination that is not directly bound to metal clusters.

Graphene transferred via electrochemical delamination

In comparison, Figure 1c shows that the graphene samples prepared via electrochemical delamination ("bubbling") exhibited a much higher amount of exposed clean monolayer area, found to be around 25% (Figure 1a, red dots) as prepared, while still having the majority of the exposed surface covered by contamination. However, annealing at only 200 °C already resulted in a level of cleanliness rivaling the 450 °C treatment from the metal-contaminated samples (Easy Transfer), and revealed atomically clean areas thousands of nm² in size. Raising the temperature to 450 °C removed almost all surface contamination, where, on average, over 90% of the free-standing areas were identified to be atomically clean. Another sample that was transferred onto a holey Si/SiN_x support and also annealed at 450 °C showed similar levels of cleanliness (Figure 1a, purple dots) as the ones transferred onto Au grids with a Quantifoil membrane. The main benefit of the rigid Si/SiN_x support is the ability to obtain large area atomically resolved images (Figure 1d) without vibrations induced by the weakening of the sample support due to the bake, manifesting as non-ideal imaging conditions and impairing the acquisition of atomic resolution images. This is further discussed in the Supporting Information.

The remaining residues after annealing at 450 °C consist mainly of copper, but also iron nanoclusters (Supplementary Figure S8, Supporting Information), embedded in carbon-rich contamination, primarily located at graphene grain boundaries, shown in Figure 2a. These metal clusters also form aggregates with a higher density of metallic residue, which are not necessarily attached to grain boundaries as seen in Figure 2b, from which dendritic carbon-rich structures appear to emerge. Supplementary Figure S9 (Supporting Information) shows that the metal contaminants are rich in Fe and Cu. We also identify nanosized holes in the material with typical sizes between 15 and 20 nm (Figure 2c). However, based on the relatively low abundance of these holes, we presume that they were already present in the material before annealing and were covered by the contamination that was removed during the heating process, instead of being annealing-induced damage. Atomically clean areas that would otherwise be thousands of nm² in size contain some isolated small carbon contamination patches (Figure 2d), likely attached to point defects in the material. Contaminants in regions where

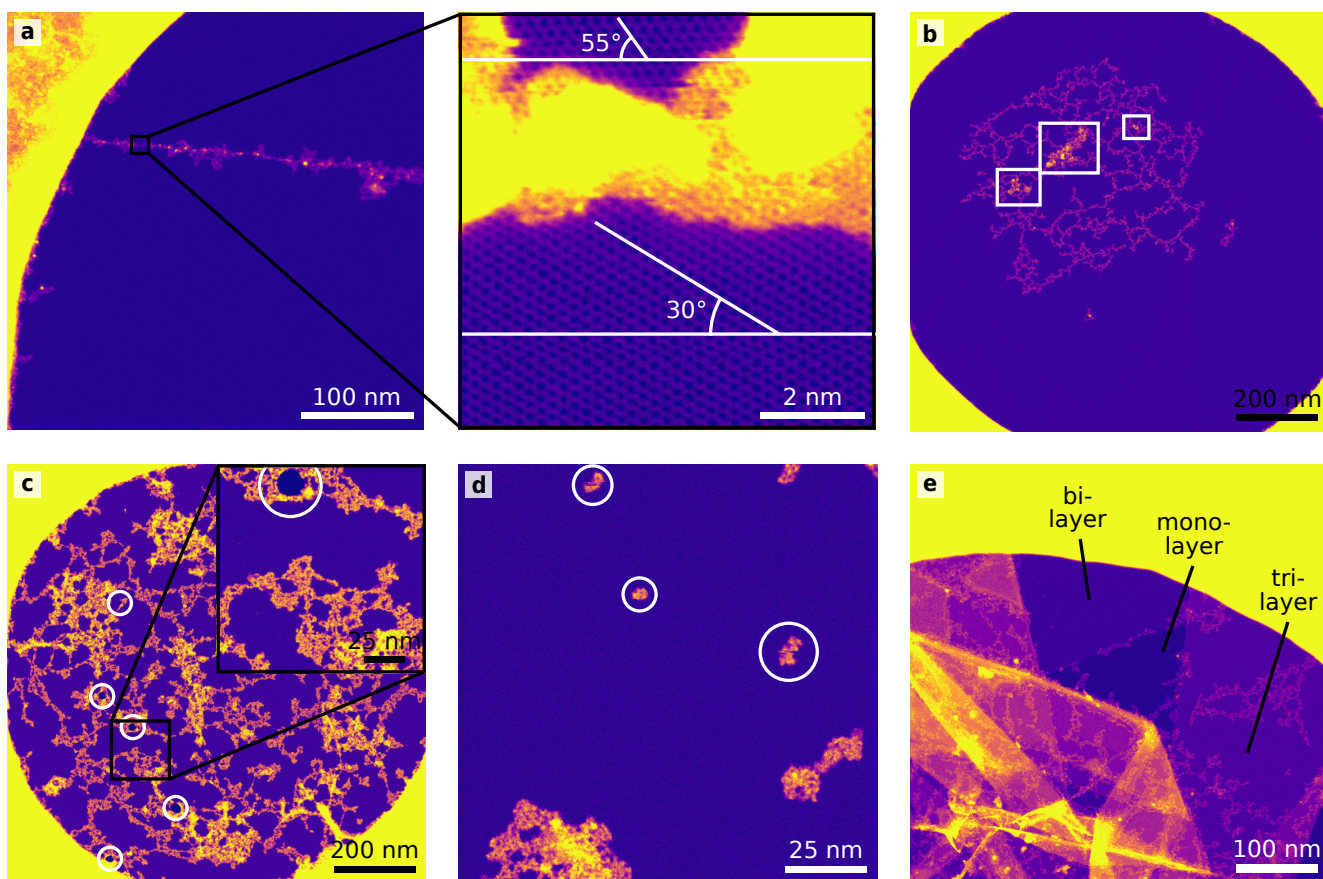


Figure 2: **MAADF-STEM images of the main cleaning limitations on graphene.** a) Grain boundary that is covered in hydrocarbon and metallic contamination, with large areas of clean graphene on both sides of the grain boundary. b) Aggregate of metal clusters (white rectangles) with dendritic hydrocarbon contamination anchored to it. c) Nanosized holes (white circles) with dendritic contamination structures around them. d) Small carbon-rich islands (white circles) embedded in what would otherwise be large clean areas. The observed streaking in the contamination islands is electron-beam-induced. e) Transfer-induced folds in graphene. The folded regions (lower left quadrant) are generally dirtier than mono- and bilayer regions, possibly due to a combination of their higher surface energy and potential contaminants trapped between the layers. The samples were annealed at a,b,e) 450 °C and c,d) 200 °C, respectively. Contrast has been adjusted to highlight relevant features, and we refer to Supplementary Figure S1 for the false color grading reference.

graphene layers folded over on themselves during the sample transfer (Figure 2e) are difficult to remove due to a rise in surface energy with increasing layer number^[83], which inhibits surface contamination desorption. Additionally, contaminants could not only be on the surfaces but also in between the layers, which would make them difficult to remove, as they cannot penetrate the layers they are sandwiched between. This results in typically dirtier areas compared to monolayer regions.

Hexagonal boron nitride

Upon investigating the pre-cleaned samples, we observed that the quality of the transferred h-BN was inferior to that of graphene made via the same transfer method. Firstly, the suspended regions showed more holes and folds compared to graphene, likely originating from the transfer process. Secondly, a large fraction of the surface consisted of multilayer structures, which appeared to emerge from SiO₂ nanoclusters (Supplementary Figure S10, Supporting Information). We presume that they were introduced during the sample growth, possibly from evaporation of SiO₂ from the quartz tube during the CVD growth process^[84], rather than during storage or transfer. Together, these two sources contributed to an estimated monolayer coverage of only around 50% (Supplementary Figure S10, Supporting Information), the highest among the three h-BN suppliers considered for this study (Supplementary Figure S11, Supporting Information), compared to practically 100% for graphene, despite the similar sample preparation procedures. This is also reflected in the strong variation of measured clean monolayer area (Figure 3a) across all temperatures, which is largely due to differences in monolayer coverage per imaged area, rather than local variations in residual contamination at a given temperature.

The as-prepared sample, where we measured an average clean area of only around 10% (Figure 3a), was annealed at 200 °C (Figure 3b), after which around 30% of the free-standing area was identified to be atomically clean monolayer h-BN. An example of atomically clean and defect-free h-BN annealed at 200 °C is shown in Figure 3c. In addition to contaminants adhered to the step edges between monolayer and bilayer regions, large portions of the surface are covered by networks of carbonaceous contamination with embedded clean areas in the range of only hundreds of nm². These networks appeared to become more and more fragmented as the temperature was increased to 250 °C and 300 °C without substantially increasing the total clean area. Only when raising the temperature to 400 °C or higher did these networks disappear across all imaged suspended monolayer areas in the sample, and the fraction of the clean suspended monolayer area approached 50%. We note that, accounting for the estimated relative free-standing monolayer area of ca. 50%, the monolayer areas exhibit a cleanliness approaching 100%, similar to what we found for graphene transferred via the same

transfer method, annealed at the same temperatures. Similar to graphene, the residual observed contamination takes the form of nanosized islands, often but not always, around copper and iron nanoclusters (Supplementary Figure S8). We also identify many small carbon-rich contamination agglomerations devoid of metallic residues within otherwise clean areas, which are likely attached to point defects in the material. However, the much higher density of these islands compared to what we found in graphene made via the same transfer method suggests a higher defect density of our transferred h-BN. While no systematic study was carried out here to characterize the defect density before or after the annealing steps, we did not observe a higher defect density in the atomically clean sites after annealing than before the treatment (Supplementary Figure S12, Supporting Information), suggesting that UHV annealing can remove the majority of the surface contamination without harming the structural integrity of free-standing monolayer h-BN in the process. The higher defect density toward the center of the frames in Supplementary Figure S12 (Supporting Information) originates from electron-beam-induced damage^[85] from prior imaging at higher local current densities to acquire the images in the insets. While it was straightforward to find atomically clean areas which were 200x200 nm² in size for graphene after the 200 °C bake, we observe a higher amount of residual contamination on h-BN that was annealed at the same temperature. The differences in the amount and morphology of contamination on h-BN and graphene after baking at only 200 °C further support a higher defect density of h-BN. While we did not investigate whether this is due to a lower quality of the source material or if the defects were introduced during sample transfer, recent literature also reported on a relatively high defect density (ca. 0.03 nm⁻²) in monolayer h-BN transferred via electrochemical delamination^[75]. Given the high thermal stability of h-BN^[86,87], and the lack of reactive species in our annealing atmosphere, in conjunction with only a modest annealing temperature, we presume that the 200 °C bake was not the source of our observed defects.

Recontaminated graphene sample

To get a better understanding of the removal of only airborne (not polymer-induced) contamination, a cleaned graphene sample that was previously heated to 450 °C (Figure 4a) was removed from the UHV system for 15 min, during which

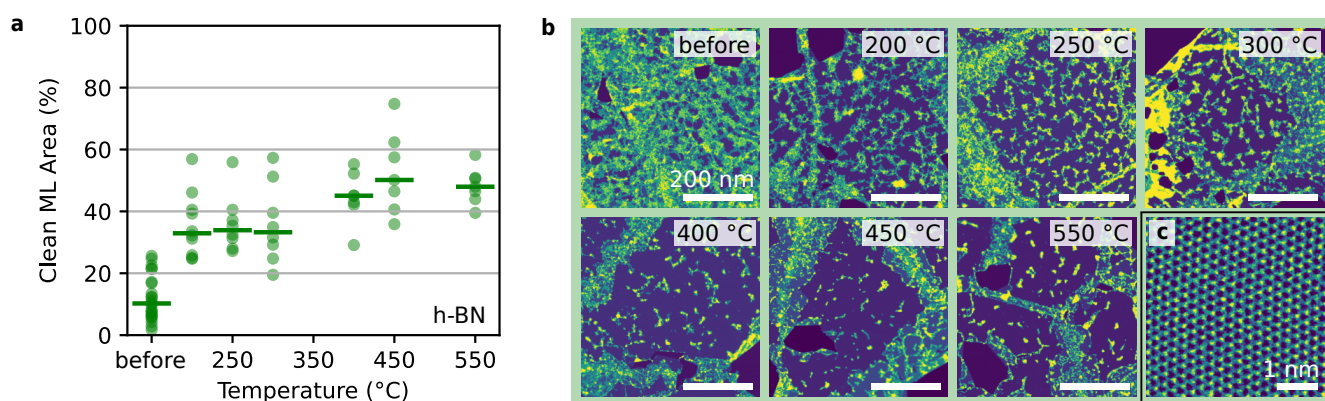


Figure 3: **h-BN cleanliness after annealing at different temperatures.** a) Relative clean monolayer (ML) area as a function of annealing temperature for h-BN. Each dot (up to ten per temperature) represents the relative amount of clean monolayer area in an imaged hole in the sample support. The horizontal bars show the median. b) Cropped MAADF-STEM images showing typical regions of free-standing monolayer h-BN before and after annealing at different temperatures. The darkest contrast is holes in the material, the second darkest contrast is clean monolayer h-BN, and the brighter features are multilayer structures and contamination. c) Gaussian filtered ($\sigma = 3$) MAADF-STEM image of pristine monolayer h-BN after annealing at 200 °C. The non-ideal imaging conditions are attributed to residual heat and vibrations originating from heating-induced thinning of the sample support. Scale bars: b) 200 nm, c) 1 nm. The non-cropped images of the frames shown in panel b) can be found in Supplementary Figure S7. Contrast has been adjusted to highlight relevant features, and we refer to Supplementary Figure S1 for the false color grading reference.

it was exposed to ambient laboratory air, but not to polymers. After re-introducing it into UHV through the regular ca. 160 °C vacuum bake overnight, the sample was found to again be heavily contaminated, with practically all of the surface being covered by hydrocarbon species (Figure 4b). However, Figure 4c shows that re-heating the sample to 200 °C already revealed more clean areas than the previous 200 °C bake (Figure 1c), where the contamination also consisted of PMMA residue. Then, the temperature was iteratively increased to higher values. While raising the temperature to 250 °C (Figure 4d) did not increase the clean area, and 300 °C (Figure 4e) provided only modest improvements, uncovering more and more of the pristine graphene lattice, it was only at 350 °C (Figure 4f) that the sample exhibited the same level of cleanliness as after the previous 450 °C bake. This can be explained by the lack of required depolymerization of the PMMA, which is initiated by the breaking of the backbone of the PMMA, reportedly occurring between 350 °C and 400 °C^[27,42,49,88], as the polymer residue had been removed by the previous 450 °C bake (before removal from UHV), with mostly airborne hydrocarbons on the surface after the re-contamination step.

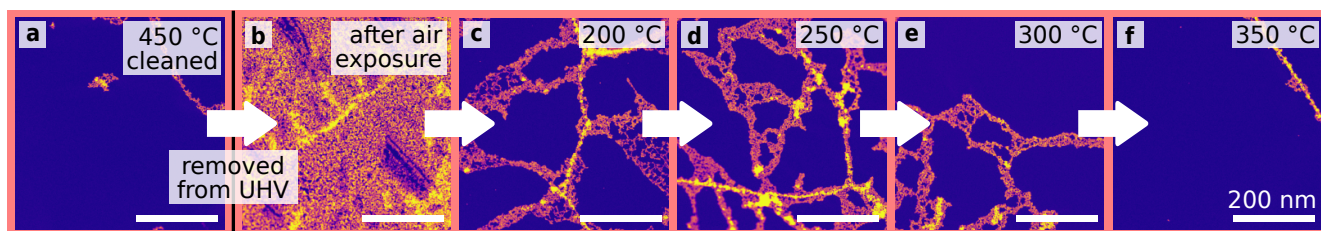


Figure 4: **Cropped MAADF-STEM images showing the heating response of a recontaminated sample.** a) Graphene sample prepared via electrochemical delamination that was cleaned at 450 °C for 3 h. b) The same sample, now full of contamination again, after removing it from UHV for 15 min followed by a 160 °C bake for over 10 h as part of the sample loading procedure. It was then iteratively heated at c) 200 °C, d) 250 °C, e) 300 °C, and f) 350 °C for 3 h each, until it exhibited the same level of cleanliness as before the recontamination step. In all images, the darkest contrast is clean monolayer graphene. Scale bars: 200 nm. The non-cropped images can be found in Supplementary Figure S7. Contrast has been adjusted to highlight relevant features, and we refer to Supplementary Figure S1 for the false color grading reference.

Conclusions

We report that thermal annealing in UHV is an effective method to remove airborne hydrocarbon and polymer contamination from both graphene and h-BN surfaces without compromising the integrity of the materials. Even annealing at temperatures as low as 200 °C can lead to noticeable contamination removal, especially when there is no polymer or metallic residue present, where well over 50% of the probed free-standing monolayer surface is identified as atomically clean. This lower annealing temperature can be a viable cleaning step for fundamental study and manipulation of 2D materials, including impurity atom implantation and defect-engineering, where heating the specimen to higher temperatures might not be necessary or possible, and may only amplify the effect of the mismatch of the thermal expansion coefficient of the material and sample support, resulting in excess strain, induced corrugations, and tearing of the material. However, heating to higher temperatures is needed to achieve cleaner surfaces as the cleaning mechanism is incomplete until the materials are annealed at over 400 °C, where the decomposition and subsequent desorption of PMMA introduced during the sample transfer has occurred, and almost all of the contamination is removed. There, we find that achieving a higher degree of cleanliness is predominantly limited by defects in the material, such as grain boundaries and point defects, as well as residual metal clusters introduced during the sample growth and transfer processes. A high amount of metallic residue can be detrimental to the achievable cleanliness, as we found that a sample mostly devoid of metal clusters,

when annealed at only 200 °C, can exhibit similar levels of cleanliness as a heavily metal-contaminated one that is baked at over 450 °C. Hence, we suggest to avoid using metal-based etchants during the sample transfer without further steps to dissolve the metallic residue, which UHV annealing cannot remove. Also, when there are no polymer residues on the surface, we obtain cleaner surfaces at lower annealing temperatures, where heating graphene to 350 °C was sufficient in obtaining atomically clean areas thousands of nm² in size, compared to over 400 °C if there was polymer present.

We also conclude that h-BN exhibits a thermal response to surface cleaning in UHV that is comparable to graphene. At temperatures above 400 °C, the surfaces are almost fully devoid of contamination, with contamination anchored to defect sites and metal clusters being the main limitation, similar to graphene. However, the quality of the material used in this work was found to be vastly inferior to that of graphene when samples transferred using the same transfer method were compared. Not only does the high abundance of multilayer structures originating from the growth heavily limit the amount of monolayer h-BN, but we also presume that the smaller average grain sizes of h-BN compared to graphene cause more damage to the material during the transfer. The resulting multilayer structures from the material folding over, covering up what would otherwise have been pristine monolayer regions, and inhibit contamination removal.

Finally, we observe only a minimal to no increase in defects for both graphene and h-BN after annealing, further reinforcing that UHV annealing can reliably clean surfaces without unintended defect creation. These large, clean surfaces can be beneficial for applications requiring large pristine areas, or for subsequent nanoscale engineering steps like defect-engineering and doping, all of which benefit from large exposed clean areas to not only increase the likelihood of interacting with the material rather than contamination, but to also utilize the improved physical properties of contamination-free 2D materials. Extending this cleaning procedure to other classes of 2D materials with different defect tolerances and less thermal stability, such as transition metal dichalcogenides^[89–91], is an important next step in evaluating its applicability for a broader range of materials, as we find that temperatures above 400 °C are necessary to remove polymer contamination from graphene and h-BN, resulting in nearly residue-free, pristine surfaces.

Acknowledgments

We thank Lukas Eminger from Lithoz for his assistance with the design of the ceramic oven, and Lithoz for providing the 3D-printed oven components. This research was funded in part by the Austrian Science Fund (FWF) [10.55776/COE5, 10.55776/DOC142, 10.55776/P35318]. For open-access purposes, the author has applied a CC-BY public copyright license to any author-accepted manuscript version arising from this submission.

Author contribution

P.I., D.L., and C.M. designed the UHV heating chamber, with further contribution from C.S. and M.L. when integrating it into the UHV system. S.C. and P.I. developed and integrated the sample transfer process, with P.I. also preparing the samples. T.A.B. prepared further hexagonal boron nitride samples used for testing the UHV heating stage. P.I. carried out the imaging for all samples. P.I. and D.L. conceptualized the data analysis methodology, with P.I. conducting the data analysis. J.K. and L.F. supervised the study. The manuscript text was initially written by P.I., and improved upon by all authors.

Data availability statement

The experimental data supporting these findings will be openly available at PHAIDRA at <https://phaidra.univie.ac.at/o:2149991> upon publication^[92].

Supporting Information

See Supporting Information for additional discussion regarding electron-beam-induced hydrocarbon deposition, sample support comparison, applied false color grading of ADF-STEM images, and a thorough description of the digital image processing steps. Additional figures on the MAADF-STEM image acquisition process, EEL spectra of metal and SiO₂ contaminants, h-BN supplier comparison and defect observations, and design sketches of the UHV heating chamber are also provided.

References

- [1] Y. Dan, Y. Lu, N. J. Kybert, Z. Luo, and A. T. Johnson. Intrinsic response of graphene vapor sensors. *Nano Letters* **9** (2009), 1472–1475. DOI: 10.1021/nl8033637.
- [2] A. Pirkle, J. Chan, A. Venugopal, D. Hinojos, C. W. Magnuson, S. McDonnell, L. Colombo, E. M. Vogel, R. S. Ruoff, and R. M. Wallace. The effect of chemical residues on the physical and electrical properties of chemical vapor deposited graphene transferred to SiO₂. *Applied Physics Letters* **99** (2011), 122108. DOI: 10.1063/1.3643444.
- [3] J. W. Suk, W. H. Lee, J. Lee, H. Chou, R. D. Piner, Y. Hao, D. Akinwande, and R. S. Ruoff. Enhancement of the Electrical Properties of Graphene Grown by Chemical Vapor Deposition via Controlling the Effects of Polymer Residue. *Nano Letters* **13** (2013), 1462–1467. DOI: 10.1021/nl304420b.
- [4] Z. Li, Y. Wang, A. Kozbial, G. Shenoy, F. Zhou, R. McGinley, P. Ireland, B. Morganstein, A. Kunkel, S. P. Surwade, L. Li, and H. Liu. Effect of airborne contaminants on the wettability of supported graphene and graphite. *Nature Materials* **12** (2013), 925–931. DOI: 10.1038/nmat3709.
- [5] M. T. Pettes, I. Jo, Z. Yao, and L. Shi. Influence of Polymeric Residue on the Thermal Conductivity of Suspended Bilayer Graphene. *Nano Letters* **11** (2011), 1195–1200. DOI: 10.1021/nl104156y.
- [6] I. Jo, M. T. Pettes, J. Kim, K. Watanabe, T. Taniguchi, Z. Yao, and L. Shi. Thermal Conductivity and Phonon Transport in Suspended Few-Layer Hexagonal Boron Nitride. *Nano Letters* **13** (2013), 550–554. DOI: 10.1021/nl304060g.
- [7] P. L. Levesque, S. S. Sabri, C. M. Aguirre, J. Guillemette, M. Siaj, P. Desjardins, T. Szkopek, and R. Martel. Probing Charge Transfer at Surfaces Using Graphene Transistors. *Nano Letters* **11** (2011), 132–137. DOI: 10.1021/nl103015w.
- [8] L. Lin, J. Zhang, H. Su, J. Li, L. Sun, Z. Wang, F. Xu, C. Liu, S. Lopatin, Y. Zhu, K. Jia, S. Chen, D. Rui, J. Sun, R. Xue, P. Gao, N. Kang, Y. Han, H. Q. Xu, Y. Cao, K. S. Novoselov, Z. Tian, B. Ren, H. Peng, and Z. Liu. Towards super-clean graphene. *Nature Communications* **10** (2019), 1912. DOI: 10.1038/s41467-019-09565-4.
- [9] A. Trentino, J. Madsen, A. Mittelberger, C. Mangler, T. Susi, K. Mustonen, and J. Kotakoski. Atomic-Level Structural Engineering of Graphene on a Mesoscopic Scale. *Nano Letters* **21** (2021), 5179–5185. DOI: 10.1021/acs.nanolett.1c01214.
- [10] C. Lee, X. Wei, J. W. Kysar, and J. Hone. Measurement of the Elastic Properties and Intrinsic Strength of Monolayer Graphene. *Science* **321** (2008), 385–388. DOI: 10.1126/science.1157996.
- [11] M. Neumann, X. Wei, L. Morales-Inostroza, S. Song, S.-G. Lee, K. Watanabe, T. Taniguchi, S. Götzinger, and Y. H. Lee. Organic Molecules as Origin of Visible-Range Single Photon Emission from Hexagonal Boron Nitride and Mica. *ACS Nano* **17** (2023), 11679–11691. DOI: 10.1021/acsnano.3c02348.
- [12] E. C. Kohlrausch, S. Ghaderzadeh, G. N. Aliev, I. Popov, F. Saad, E. Alharbi, Q. M. Ramasse, G. A. Rance, M. Danaie, M. Thangamuthu, M. Young, R. Plummer, D. J. Morgan, W. Theis, E. Besley, A. N. Khlobystov, and J. Alves Fernandes. One-Size-Fits-All: A Universal Binding Site for Single-Layer Metal Cluster Self-Assembly. *Advanced Science* (2025), e08034. DOI: 10.1002/advs.202508034.
- [13] W. Joudi, R. S. Windisch, A. Trentino, D. Propst, J. Madsen, T. Susi, C. Mangler, K. Mustonen, F. Libisch, and J. Kotakoski. Corrugation-Dominated Mechanical Softening of Defect-Engineered Graphene. *Physical Review Letters* **134** (2025), 166102. DOI: 10.1103/PhysRevLett.134.166102.
- [14] W. Joudi, S. Ghaderzadeh, A. Trentino, K. Mizohata, K. Mustonen, E. Besley, J. Kotakoski, and E. H. Åhlgren. Two-Dimensional One-Atom-Thick Gold Grown on Defect-Engineered Graphene. *ACS Nano* **19** (2025), 22032–22043. DOI: 10.1021/acsnano.5c01538.
- [15] A. Grubišić-Čabo, M. Michiardi, C. E. Sanders, M. Bianchi, D. Curcio, D. Phuyal, M. H. Berntsen, Q. Guo, and M. Dendzik. In Situ Exfoliation Method of Large-Area 2D Materials. *Advanced Science* **10** (2023), 2301243. DOI: 10.1002/ADVS.202301243.
- [16] K. E. Whitener and P. E. Sheehan. Graphene synthesis. *Diamond and Related Materials* **46** (2014), 25–34. DOI: 10.1016/J.DIAMOND.2014.04.006.
- [17] Y. Ji, B. Calderon, Y. Han, P. Cueva, N. R. Jungwirth, H. A. Alsaman, J. Hwang, G. D. Fuchs, D. A. Muller, and M. G. Spencer. Chemical Vapor Deposition Growth of Large Single-Crystal Mono-, Bi-, Tri-Layer Hexagonal Boron Nitride and Their Interlayer Stacking. *ACS Nano* **11** (2017), 12057–12066. DOI: 10.1021/acsnano.7b04841.

- [18] K. Zhang, Y. Feng, F. Wang, Z. Yang, and J. Wang. Two dimensional hexagonal boron nitride (2D-hBN): synthesis, properties and applications. *Journal of Materials Chemistry C* **5** (2017), 11992–12022. DOI: 10.1039/C7TC04300G.
- [19] G. Algara-Siller, O. Lehtinen, A. Turchanin, and U. Kaiser. Dry-cleaning of graphene. *Applied Physics Letters* **104** (2014), 153115. DOI: 10.1063/1.4871997.
- [20] T. Susi, J. C. Meyer, and J. Kotakoski. Manipulating low-dimensional materials down to the level of single atoms with electron irradiation. *Ultramicroscopy* **180** (2017), 163–172. DOI: 10.1016/j.ultramicro.2017.03.005.
- [21] M. Salim, J. Hurst, M. Montgomery, N. Tolman, and H. Liu. Airborne contamination of graphite as analyzed by ultra-violet photoelectron spectroscopy. *Journal of Electron Spectroscopy and Related Phenomena* **235** (2019), 8–15. DOI: 10.1016/j.eispec.2019.06.001.
- [22] P. Schweizer, C. Dolle, D. Dasler, G. Abellán, F. Hauke, A. Hirsch, and E. Spiecker. Mechanical cleaning of graphene using in situ electron microscopy. *Nature Communications* **2020 11:1 11** (2020), 1–9. DOI: 10.1038/s41467-020-15255-3.
- [23] A. Reina, H. Son, L. Jiao, B. Fan, M. S. Dresselhaus, Z. Liu, and J. Kong. Transferring and Identification of Single- and Few-Layer Graphene on Arbitrary Substrates. *The Journal of Physical Chemistry C* **112** (2008), 17741–17744. DOI: 10.1021/jp807380s.
- [24] L. Jiao, B. Fan, X. Xian, Z. Wu, J. Zhang, and Z. Liu. Creation of Nanostructures with Poly(methyl methacrylate)-Mediated Nanotransfer Printing. *Journal of the American Chemical Society* **130** (2008), 12612–12613. DOI: 10.1021/ja805070b.
- [25] Z. Cheng, Q. Zhou, C. Wang, Q. Li, C. Wang, and Y. Fang. Toward Intrinsic Graphene Surfaces: A Systematic Study on Thermal Annealing and Wet-Chemical Treatment of SiO₂-Supported Graphene Devices. *Nano Letters* **11** (2011), 767–771. DOI: 10.1021/nl103977d.
- [26] Y.-C. Lin, C. Jin, J.-C. Lee, S.-F. Jen, K. Suenaga, and P.-W. Chiu. Clean Transfer of Graphene for Isolation and Suspension. *ACS Nano* **5** (2011), 2362–2368. DOI: 10.1021/nn200105j.
- [27] W. Xie, L.-T. Weng, K. M. Ng, C. K. Chan, and C.-M. Chan. Clean graphene surface through high temperature annealing. *Carbon* **94** (2015), 740–748. DOI: 10.1016/j.carbon.2015.07.046.
- [28] G. Cunge, D. Ferrah, C. Petit-Etienne, A. Davydova, H. Okuno, D. Kalita, V. Bouchiat, and O. Renault. Dry efficient cleaning of poly-methyl-methacrylate residues from graphene with high-density H₂ and H₂-N₂ plasmas. *Journal of Applied Physics* **118** (2015), 123302. DOI: 10.1063/1.4931370.
- [29] L. Sun, L. Lin, Z. Wang, D. Rui, Z. Yu, J. Zhang, Y. Li, X. Liu, K. Jia, K. Wang, L. Zheng, B. Deng, T. Ma, N. Kang, H. Xu, K. S. Novoselov, H. Peng, and Z. Liu. A Force-Engineered Lint Roller for Superclean Graphene. *Advanced Materials* **31** (2019), 1902978. DOI: 10.1002/adma.201902978.
- [30] J. Sun, H. O. Finklea, and Y. Liu. Characterization and electrolytic cleaning of poly(methyl methacrylate) residues on transferred chemical vapor deposited graphene. *Nanotechnology* **28** (2017), 125703–125703. DOI: 10.1088/1361-6528/AA5E55.
- [31] J.-N. Longchamp, C. Escher, and H.-W. Fink. Ultraclean freestanding graphene by platinum-metal catalysis. *Journal of Vacuum Science & Technology B* **31** (2013), 020605. DOI: 10.1116/1.4793746.
- [32] A. Yulaev, G. Cheng, A. R. H. Walker, I. V. Vlassiouk, A. Myers, M. S. Leite, and A. Kolmakov. Toward clean suspended CVD graphene. *RSC Advances* **6** (2016), 83954–83962. DOI: 10.1039/C6RA17360H.
- [33] B. Zhuang, S. Li, S. Li, and J. Yin. Ways to eliminate PMMA residues on graphene — superclean graphene. *Carbon* **173** (2021), 609–636. DOI: 10.1016/j.carbon.2020.11.047.
- [34] N. Lindvall, A. Kalabukhov, and A. Yurgens. Cleaning graphene using atomic force microscope. *Journal of Applied Physics* **111** (2012), 064904. DOI: 10.1063/1.3695451.
- [35] D. Ferrah, O. Renault, C. Petit-Etienne, H. Okuno, C. Berne, V. Bouchiat, and G. Cunge. XPS investigations of graphene surface cleaning using H₂- and Cl₂-based inductively coupled plasma. *Surface and Interface Analysis* **48** (2016), 451–455. DOI: 10.1002/sia.6010.
- [36] D. Ferrah, O. Renault, D. Marinov, J. Arias-Zapata, N. Chevalier, D. Mariolle, D. Rouchon, H. Okuno, V. Bouchiat, and G. Cunge. CF₄/H₂ Plasma Cleaning of Graphene Regenerates Electronic Properties of the Pristine Material. *ACS Applied Nano Materials* **2** (2019), 1356–1366. DOI: 10.1021/acsanm.8b02249.

- [37] Y. Jia, X. Gong, P. Peng, Z. Wang, Z. Tian, L. Ren, Y. Fu, and H. Zhang. Toward High Carrier Mobility and Low Contact Resistance: Laser Cleaning of PMMA Residues on Graphene Surfaces. *Nano-Micro Letters* **8** (2016), 336–346. DOI: 10.1007/s40820-016-0093-5.
- [38] M. Tripathi, A. Mittelberger, K. Mustonen, C. Mangler, J. Kotakoski, J. C. Meyer, and T. Susi. Cleaning graphene: Comparing heat treatments in air and in vacuum. *physica status solidi (RRL) – Rapid Research Letters* **11** (2017), 1700124. DOI: 10.1002/pssr.201700124.
- [39] J. Moser, A. Barreiro, and A. Bachtold. Current-induced cleaning of graphene. *Applied Physics Letters* **91** (2007), 163513. DOI: 10.1063/1.2789673.
- [40] K. I. Bolotin, K. J. Sikes, Z. Jiang, M. Klima, G. Fudenberg, J. Hone, P. Kim, and H. L. Stormer. Ultrahigh electron mobility in suspended graphene. *Solid State Communications* **146** (2008), 351–355. DOI: 10.1016/j.ssc.2008.02.024.
- [41] H. Wang, X. Zhang, and H. Takamatsu. Ultraclean suspended monolayer graphene achieved by in situ current annealing. *Nanotechnology* **28** (2016), 045706. DOI: 10.1088/1361-6528/28/4/045706.
- [42] Y. Ahn, H. Kim, Y. H. Kim, Y. Yi, and S. I. Kim. Procedure of removing polymer residues and its influences on electronic and structural characteristics of graphene. *Applied Physics Letters* **102** (2013), 091602. DOI: 10.1063/1.4794900.
- [43] K. Kumar, Y. S. Kim, and E. H. Yang. The influence of thermal annealing to remove polymeric residue on the electronic doping and morphological characteristics of graphene. *Carbon* **65** (2013), 35–45. DOI: 10.1016/J.CARBON.2013.07.088.
- [44] Y.-C. Lin, C.-C. Lu, C.-H. Yeh, C. Jin, K. Suenaga, and P.-W. Chiu. Graphene Annealing: How Clean Can It Be? *Nano Letters* **12** (2012), 414–419. DOI: 10.1021/nl203733r.
- [45] C. Gong, H. C. Floresca, D. Hinojos, S. McDonnell, X. Qin, Y. Hao, S. Jandhyala, G. Mordi, J. Kim, L. Colombo, R. S. Ruoff, M. J. Kim, K. Cho, R. M. Wallace, and Y. J. Chabal. Rapid Selective Etching of PMMA Residues from Transferred Graphene by Carbon Dioxide. *The Journal of Physical Chemistry C* **117** (2013), 23000–23008. DOI: 10.1021/jp408429v.
- [46] W. Choi, Y. S. Seo, J. Y. Park, K. B. Kim, J. Jung, N. Lee, Y. Seo, and S. Hong. Effect of annealing in Ar/H₂ environment on chemical vapor deposition-grown graphene transferred with poly (Methyl Methacrylate). *IEEE Transactions on Nanotechnology* **14** (2015), 70–74. DOI: 10.1109/TNANO.2014.2365208.
- [47] X. Wang, A. Dolocan, H. Chou, L. Tao, A. Dick, D. Akinwande, and C. G. Willson. Direct Observation of Poly(Methyl Methacrylate) Removal from a Graphene Surface. *Chemistry of Materials* **29** (2017), 2033–2039. DOI: 10.1021/acs.chemmater.6b03875.
- [48] L. H. Karlsson, J. Birch, A. Mockute, A. S. Ingason, H. Q. Ta, M. H. Rummeli, J. Rosen, and P. O. Persson. Graphene on graphene formation from PMMA residues during annealing. *Vacuum* **137** (2017), 191–194. DOI: 10.1016/J.VACUUM.2017.01.004.
- [49] Y. Ahn, J. Kim, S. Ganorkar, Y.-H. Kim, and S.-I. Kim. Thermal annealing of graphene to remove polymer residues. *Materials Express* **6** (2016), 69–76. DOI: 10.1166/mex.2016.1272.
- [50] J. Hong, M. K. Park, E. J. Lee, D. Lee, D. S. Hwang, and S. Ryu. Origin of New Broad Raman D and G Peaks in Annealed Graphene. *Scientific Reports* **3** (2013), 2700. DOI: 10.1038/srep02700.
- [51] L.-W. Huang, C.-K. Chang, F.-C. Chien, K.-H. Chen, P. Chen, F.-R. Chen, and C.-S. Chang. Characterization of the cleaning process on a transferred graphene. *Journal of Vacuum Science & Technology A* **32** (2014), 050601. DOI: 10.1116/1.4886735.
- [52] J. Zhang, K. Jia, L. Lin, W. Zhao, H. T. Quang, L. Sun, T. Li, Z. Li, X. Liu, L. Zheng, R. Xue, J. Gao, Z. Luo, M. H. Rummeli, Q. Yuan, H. Peng, and Z. Liu. Large-Area Synthesis of Superclean Graphene via Selective Etching of Amorphous Carbon with Carbon Dioxide. *Angewandte Chemie International Edition* **58** (2019), 14446–14451. DOI: 10.1002/anie.201905672.
- [53] A. Siokou, F. Ravani, S. Karakalos, O. Frank, M. Kalbac, and C. Galotis. Surface refinement and electronic properties of graphene layers grown on copper substrate: An XPS, UPS and EELS study. *Applied Surface Science* **257** (2011), 9785–9790. DOI: 10.1016/j.apsusc.2011.06.017.

- [54] K. R. Paserba and A. J. Gellman. Kinetics and energetics of oligomer desorption from surfaces. *Physical Review Letters* **86** (2001), 4338–4341. DOI: 10.1103/PhysRevLett.86.4338.
- [55] E. Londero, E. K. Karlson, M. Landahl, D. Ostrovskii, J. D. Rydberg, and E. Schröder. Desorption of n-alkanes from graphene: a van der Waals density functional study. *Journal of Physics: Condensed Matter* **24** (2012), 424212. DOI: 10.1088/0953-8984/24/42/424212.
- [56] K. K. Kim, A. Hsu, X. Jia, S. M. Kim, Y. Shi, M. Dresselhaus, T. Palacios, and J. Kong. Synthesis and Characterization of Hexagonal Boron Nitride Film as a Dielectric Layer for Graphene Devices. *ACS Nano* **6** (2012), 8583–8590. DOI: 10.1021/nn301675f.
- [57] M. Okada, T. Sawazaki, K. Watanabe, T. Taniguchi, H. Hibino, H. Shinohara, and R. Kitaura. Direct Chemical Vapor Deposition Growth of WS₂ Atomic Layers on Hexagonal Boron Nitride. *ACS Nano* **8** (2014), 8273–8277. DOI: 10.1021/nn503093k.
- [58] S. M. Kim, A. Hsu, M. H. Park, S. H. Chae, S. J. Yun, J. S. Lee, D.-H. Cho, W. Fang, C. Lee, T. Palacios, M. Dresselhaus, K. K. Kim, Y. H. Lee, and J. Kong. Synthesis of large-area multilayer hexagonal boron nitride for high material performance. *Nature Communications* **6** (2015), 8662. DOI: 10.1038/ncomms9662.
- [59] S. K. Jang, J. Youn, Y. J. Song, and S. Lee. Synthesis and Characterization of Hexagonal Boron Nitride as a Gate Dielectric. *Scientific Reports* **6** (2016), 30449. DOI: 10.1038/srep30449.
- [60] A. Yan, J. J. Velasco, S. Kahn, K. Watanabe, T. Taniguchi, F. Wang, M. F. Crommie, and A. Zettl. Direct Growth of Single- and Few-Layer MoS₂ on h-BN with Preferred Relative Rotation Angles. *Nano Letters* **15** (2015), 6324–6331. DOI: 10.1021/acs.nanolett.5b01311.
- [61] R. Bourrellier, S. Meuret, A. Tararan, O. Stéphan, M. Kociak, L. H. G. Tizei, and A. Zobelli. Bright UV Single Photon Emission at Point Defects in h-BN. *Nano Letters* **16** (2016), 4317–4321. DOI: 10.1021/acs.nanolett.6b01368.
- [62] T. T. Tran, K. Bray, M. J. Ford, M. Toth, and I. Aharonovich. Quantum emission from hexagonal boron nitride monolayers. *Nature Nanotechnology* **11** (2016), 37–41. DOI: 10.1038/nnano.2015.242.
- [63] A. Gottscholl, M. Kianinia, V. Soltamov, S. Orlinskii, G. Mamin, C. Bradac, C. Kasper, K. Krambrock, A. Sperlich, M. Toth, I. Aharonovich, and V. Dyakonov. Initialization and read-out of intrinsic spin defects in a van der Waals crystal at room temperature. *Nature Materials* **19** (2020), 540–545. DOI: 10.1038/s41563-020-0619-6.
- [64] A. Sajid, M. J. Ford, and J. R. Reimers. Single-photon emitters in hexagonal boron nitride: a review of progress. *Reports on Progress in Physics* **83** (2020), 044501. DOI: 10.1088/1361-6633/ab6310.
- [65] G.-L. Liu, X.-Y. Wu, P.-T. Jing, Z. Cheng, D. Zhan, Y. Bao, J.-X. Yan, H. Xu, L.-G. Zhang, B.-H. Li, K.-W. Liu, L. Liu, and D.-Z. Shen. Single Photon Emitters in Hexagonal Boron Nitride Fabricated by Focused Helium Ion Beam. *Advanced Optical Materials* **12** (2024), 2302083. DOI: 10.1002/adom.202302083.
- [66] T. T. Tran, C. Elbadawi, D. Totonjian, C. J. Lobo, G. Grosso, H. Moon, D. R. Englund, M. J. Ford, I. Aharonovich, and M. Toth. Robust Multicolor Single Photon Emission from Point Defects in Hexagonal Boron Nitride. *ACS Nano* **10** (2016), 7331–7338. DOI: 10.1021/acs.nano.6b03602.
- [67] G. Grosso, H. Moon, B. Lienhard, S. Ali, D. K. Efetov, M. M. Furchi, P. Jarillo-Herrero, M. J. Ford, I. Aharonovich, and D. Englund. Tunable and high-purity room temperature single-photon emission from atomic defects in hexagonal boron nitride. *Nature Communications* **8** (2017), 705. DOI: 10.1038/s41467-017-00810-2.
- [68] T. W. Tang, R. Ritika, M. Tamtaji, H. Liu, Y. Hu, Z. Liu, P. R. Galligan, M. Xu, J. Shen, J. Wang, J. You, Y. Li, G. Chen, I. Aharonovich, and Z. Luo. Structured-Defect Engineering of Hexagonal Boron Nitride for Identified Visible Single-Photon Emitters. *ACS Nano* **19** (2025), 8509–8519. DOI: 10.1021/acs.nano.4c11413.
- [69] M. Mackoitis-Sinkevičienė, M. Maciaszek, C. G. Van de Walle, and A. Alkauskas. Carbon dimer defect as a source of the 4.1 eV luminescence in hexagonal boron nitride. *Applied Physics Letters* **115** (2019), 212101. DOI: 10.1063/1.5124153.
- [70] N. Mendelson, D. Chugh, J. R. Reimers, T. S. Cheng, A. Gottscholl, H. Long, C. J. Mellor, A. Zettl, V. Dyakonov, P. H. Beton, S. V. Novikov, C. Jagadish, H. H. Tan, M. J. Ford, M. Toth, C. Bradac, and I. Aharonovich. Identifying carbon as the source of visible single-photon emission from hexagonal boron nitride. *Nature Materials* **20** (2021), 321–328. DOI: 10.1038/s41563-020-00850-y.

- [71] F. Ren and Z. Xu. Atomistic Simulations of Carbon Implantation into hBN for Creating Color Centers. *The Journal of Physical Chemistry C* **129** (2025), 5054–5064. DOI: 10.1021/acs.jpcc.4c07558.
- [72] A. G. F. Garcia, M. Neumann, F. Amet, J. R. Williams, K. Watanabe, T. Taniguchi, and D. Goldhaber-Gordon. Effective Cleaning of Hexagonal Boron Nitride for Graphene Devices. *Nano Letters* **12** (2012), 4449–4454. DOI: 10.1021/nl3011726.
- [73] C. M. Orofeo, S. Suzuki, and H. Hibino. Ultrathin Chemical Vapor Deposition (CVD)-Grown Hexagonal Boron Nitride as a High-Quality Dielectric for Tunneling Devices on Rigid and Flexible Substrates. *The Journal of Physical Chemistry C* **118** (2014), 3340–3346. DOI: 10.1021/jp410874z.
- [74] S. J. Cartamil-Bueno, M. Cavalieri, R. Wang, S. Hourii, S. Hofmann, and H. S. J. van der Zant. Mechanical characterization and cleaning of CVD single-layer h-BN resonators. *npj 2D Materials and Applications* **1** (2017), 1–7. DOI: 10.1038/s41699-017-0020-8.
- [75] D. O. Byrne and F. I. Allen. Atomic Engineering of Triangular Nanopores in Monolayer hBN for Membrane Applications: A Decoupled Seeding and Growth Approach. *ACS Applied Nano Materials* **8** (2025), 4565–4572. DOI: 10.1021/acsanm.4c06998.
- [76] D. Propst, W. Joudi, M. Längle, J. Madsen, C. Kofler, B. M. Mayer, D. Lamprecht, C. Mangler, L. Filipovic, T. Susi, and J. Kotakoski. Automated image acquisition and analysis of graphene and hexagonal boron nitride from pristine to highly defective and amorphous structures. *Scientific Reports* **14** (2024), 26939. DOI: 10.1038/s41598-024-77740-9.
- [77] S. Paul, B. Das, A. Kar, S. Das, S. R. Mohanty, K. Watanabe, T. Taniguchi, S. Datta, and K. S. R. Menon. Residue-free layered material interfaces for device processing. *Applied Surface Science* **685** (2025), 161961. DOI: 10.1016/j.apsusc.2024.161961.
- [78] Y. Wang, Y. Zheng, X. Xu, E. Dubuisson, Q. Bao, J. Lu, and K. P. Loh. Electrochemical Delamination of CVD-Grown Graphene Film: Toward the Recyclable Use of Copper Catalyst. *ACS Nano* **5** (2011), 9927–9933. DOI: 10.1021/nn203700w.
- [79] C. Mangler, J. Meyer, A. Mittelberger, K. Mustonen, T. Susi, and J. Kotakoski. A Materials Scientist’s CANVAS: A System for Controlled Alteration of Nanomaterials in Vacuum Down to the Atomic Scale. *Microscopy and Microanalysis* **28** (2022), 2940–2942. DOI: 10.1017/S1431927622011023.
- [80] M. Hotz, G. Corbin, N. Dellby, O. Krivanek, C. Mangier, and J. Meyer. Ultra-High Vacuum Aberration-Corrected STEM for in-situ studies. *Microscopy and Microanalysis* **22** (2016), 34–35. DOI: 10.1017/S1431927616001021.
- [81] M. Hugenschmidt, K. Adrion, A. Marx, E. Müller, and D. Gerthsen. Electron-Beam-Induced Carbon Contamination in STEM-in-SEM: Quantification and Mitigation. *Microscopy and Microanalysis* **29** (2023), 219–234. DOI: 10.1093/micmic/ozac003.
- [82] O. Dyck, S. Kim, S. V. Kalinin, and S. Jesse. Mitigating e-beam-induced hydrocarbon deposition on graphene for atomic-scale scanning transmission electron microscopy studies. *Journal of Vacuum Science & Technology B* **36** (2017), 011801. DOI: 10.1116/1.5003034.
- [83] L. S. Kocherlakota, B. A. Krajina, and R. M. Overney. Communication: Local energetic analysis of the interfacial and surface energies of graphene from the single layer to graphite. *The Journal of Chemical Physics* **143** (2015), 241105. DOI: 10.1063/1.4939248.
- [84] I. Ruiz, W. Wang, A. George, C. S. Ozkan, and M. Ozkan. Silicon Oxide Contamination of Graphene Sheets Synthesized on Copper Substrates via Chemical Vapor Deposition. *Advanced Science, Engineering and Medicine* **6** (2014), 1070–1075. DOI: 10.1166/ase.2014.1615.
- [85] T. A. Bui, G. T. Leuthner, J. Madsen, M. R. A. Monazam, A. I. Chirita, A. Postl, C. Mangler, J. Kotakoski, and T. Susi. Creation of Single Vacancies in hBN with Electron Irradiation. *Small* **19** (2023), 2301926. DOI: 10.1002/smll.202301926.
- [86] Z. Liu, Y. Gong, W. Zhou, L. Ma, J. Yu, J. C. Idrobo, J. Jung, A. H. MacDonald, R. Vajtai, J. Lou, and P. M. Ajayan. Ultrathin high-temperature oxidation-resistant coatings of hexagonal boron nitride. *Nature Communications* **4** (2013), 2541. DOI: 10.1038/ncomms3541.
- [87] L. H. Li, J. Cervenka, K. Watanabe, T. Taniguchi, and Y. Chen. Strong Oxidation Resistance of Atomically Thin Boron Nitride Nanosheets. *ACS Nano* **8** (2014), 1457–1462. DOI: 10.1021/nn500059s.

- [88] T. Kashiwagi, A. Inaba, J. E. Brown, K. Hatada, T. Kitayama, and E. Masuda. Effects of weak linkages on the thermal and oxidative degradation of poly(methyl methacrylates). *Macromolecules* **19** (1986), 2160–2168. DOI: 10.1021/ma00162a010.
- [89] E. Pitthan, E. R. F. Gerling, T. O. Feijó, C. Radtke, and G. V. Soares. Annealing Response of Monolayer MoS₂ Grown by Chemical Vapor Deposition. *ECS Journal of Solid State Science and Technology* **8** (2019), P267. DOI: 10.1149/2.0061904jss.
- [90] P. Kumar, J. P. Horwath, A. C. Foucher, C. C. Price, N. Acero, V. B. Shenoy, E. A. Stach, and D. Jariwala. Direct visualization of out-of-equilibrium structural transformations in atomically thin chalcogenides. *npj 2D Materials and Applications* **4** (2020), 16–16. DOI: 10.1038/s41699-020-0150-2.
- [91] R. Tilmann, C. Bartlam, O. Hartwig, B. Tywoniuk, N. Dominik, C. P. Cullen, L. Peters, T. Stimpel-Lindner, N. McEvoy, and G. S. Duesberg. Identification of Ubiquitously Present Polymeric Adlayers on 2D Transition Metal Dichalcogenides. *ACS Nano* **17** (2023), 10617–10627. DOI: 10.1021/acsnano.3c01649.
- [92] P. Irschik, D. Lamprecht, S. Chokappa, C. Mangler, C. Speckmann, T. A. Bui, M. Längle, L. Filipovic, and J. Kotakoski. Raw data for the publication "Atomically clean free-standing two-dimensional materials through heating in ultra-high vacuum". *PHAIDRA* (2025). URL: <https://phaidra.univie.ac.at/detail/o:2149991>.

Supporting Information for
**Atomically clean free-standing two-dimensional materials
through heating in ultra-high vacuum**

Philipp Irschik^{1,2,*}, David Lamprecht^{1,3}, Shrirang Chokappa^{1,2}, Clemens Mangler¹, Carsten Speckmann¹, Thuy An Bui^{1,2}, Manuel Längle¹, Lado Filipovic³, Jani Kotakoski^{1,*}

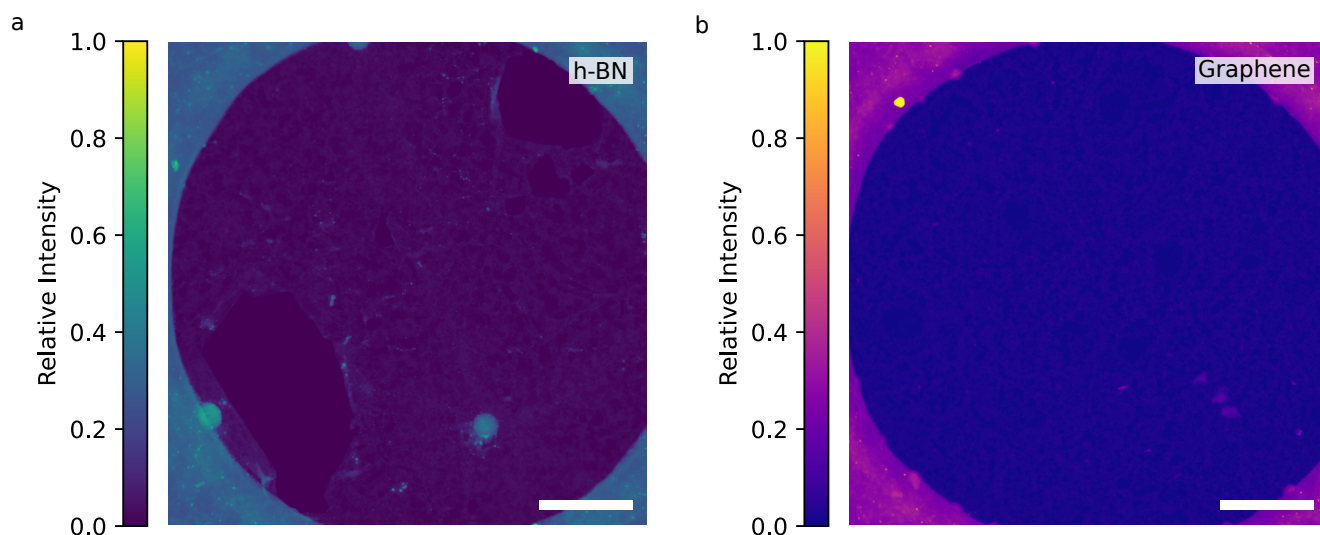
¹University of Vienna, Faculty of Physics, Boltzmanngasse 5, 1090 Vienna, Austria

²University of Vienna, Vienna Doctoral School in Physics, Boltzmanngasse 5, 1090 Vienna, Austria

³Institute for Microelectronics, TU Wien, Gußhausstraße 27-29/E360, 1040 Vienna, Austria

*Email: philipp.irschik@univie.ac.at, jani.kotakoski@univie.ac.at

August 28, 2025



Supplementary Figure S1: **Color maps used for h-BN and graphene.** Example false color MAADF-STEM images without contrast enhancement of suspended a) h-BN and b) graphene on the sample support (bright features in the corners), where the same color maps shown here were also applied to all other ADF-STEM images, both in the main text and the Supporting Information. There, the contrast was adjusted to highlight relevant features in the respective images. Scale bars: 200 nm.

Applied color maps

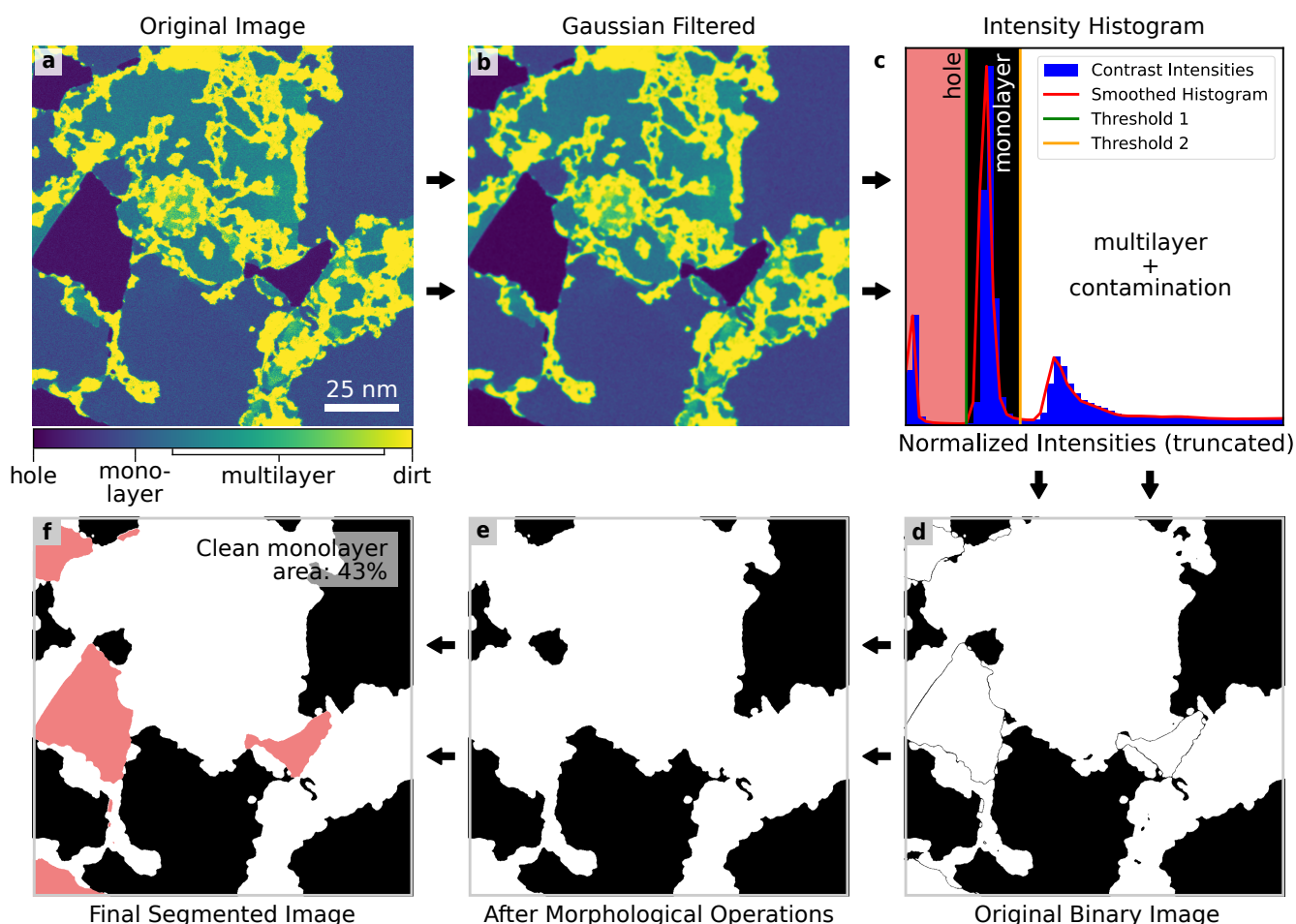
To improve the visual clarity and ease in comparability of the different sample types for the reader, false colors were applied to all ADF-STEM images of graphene and h-BN throughout the main text and the Supporting Information. Figure S1 shows example images of graphene and h-BN suspended over the holey carbon sample support (bright intensities in the corners of the images) without any contrast enhancements applied. To highlight various features in other images presented in this work, different linear contrast enhancements were applied, while keeping the false color grading the same, and we refer the reader to the color bars presented in Figure S1 for relative intensity comparisons.

Digital image processing

We identified monolayer graphene or h-BN as the darkest features in the image, or the second darkest features if the frame contains a hole. An example frame is shown in Figure S2a. To determine if a frame contains a hole, we employed an automated detection algorithm, where around ten reference images acquired during the same microscopy session that had been manually identified as containing pixels attributed to vacuum were selected as reference images. They

were subjected to a Gaussian filter (kernel size 17×17 px, $\sigma = 2$ px), from which a contrast intensity histogram (2048 bins) was generated. This histogram was iteratively smoothed using a one-dimensional Gaussian filter with a width of 3 bins ($\sigma = 0.2$) for 50 iterations. Afterwards, the peak position of the leftmost peak (lower intensity values), which corresponds to the average intensity of the noise floor in a given frame, was identified and stored as reference data. The same procedure was then carried out for all frames acquired during the same microscopy session. If the leftmost peak of an image in its corresponding histogram was within the reference data's span or within ± 3 standard deviations (whichever was greater), the image was labeled as containing a hole and subsequently added to the reference data before continuing with the next frame. This procedure was iteratively executed until no new frames were added to the reference images.

To determine the relative amount of clean monolayer area in each frame, a Gaussian filter (kernel size 17×17 px, $\sigma = 2$ px) was first applied (Figure S2b) to aid in peak detection in the normalized contrast intensity histogram (1024 bins). The resulting histogram (Figure S2c, blue bars) was iteratively smoothed using a one-dimensional Gaussian filter with a width of 3 bins ($\sigma = 0.2$) until the number of peaks reached a constant value. This smoothed histogram (Figure S2c, red line) was then thresholded using either the minimum or triangle method based on the number of identified peaks, with a difference between the two methods of typically less than 2%. This way, the intensity peak corresponding to the clean monolayer regions in the image was reliably isolated (success rate $> 95\%$) from the contamination and other higher-contrast features, such as multilayer regions, in addition to holes in the material, if applicable. The thresholds were used to generate a binary image, where the contaminated areas (and holes) were masked (Figure S2d). Subsequently, the binary image underwent a series of morphological operations, starting with an opening process with a circular kernel with a diameter of 0.5 nm (4 px), roughly corresponding to two lattice constants for both graphene and h-BN. This was done to both remove small clean areas and to separate barely connected ones (by contrast). If the image contained a hole, closing with the same kernel was performed before the opening process to close areas between the holes and the adjacent



Supplementary Figure S2: **Digital image processing steps for image thresholding and segmentation.** a) Example MAADF-STEM image used to identify clean monolayer coverage. This one contains holes (darkest contrast), clean monolayer h-BN (second darkest contrast) and bilayer structures, and contamination (brighter contrast). b) The same frame after applying a Gaussian filter (kernel size 17 px, $\sigma = 2$ px). c) Contrast intensity histogram (1024 bins total) of the image in b). The histogram is truncated (56 bins are shown) to highlight relevant features. The red line resulted from iterative histogram smoothing. The colored vertical lines mark the two intensity thresholds. d) Original binary image obtained from the double thresholding process. Clean monolayer regions are black, other features are white. e) Binary image from panel d) after closing, opening, and inverted area opening (hole-filling) to remove artifacts from the thresholding process, and to remove small clean areas. f) Final segmented image, where clean monolayer areas are black, holes are pink, and multilayer regions and contamination are white.

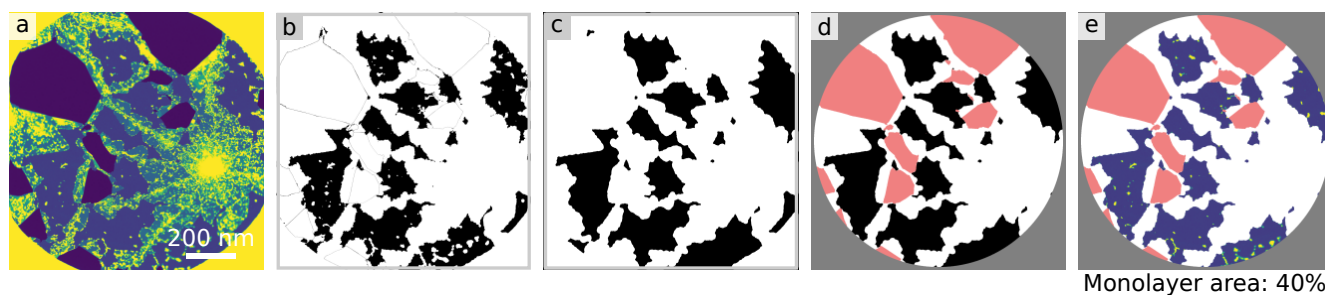
covered areas (thin black contours in Figure S2d), which had resulted from the Gaussian blur prior. Then, 8-connectivity inverted area opening (hole-filling) was performed to remove connected clean regions smaller than 16 nm^2 (1024 px^2), resulting in Figure S2e. This size threshold was chosen since areas as small as approximately 8 nm^2 have been utilized in recent literature to identify monolayer phosphorene^[1] and single phosphorus dopants in graphene^[2]. The chosen size was doubled from 8 to 16 nm^2 to account for differences in the morphology of the clean areas. Figure S2f shows the

final segmented image, where the black pixels correspond to atomically clean areas, white pixels are contamination and multilayer structures, and pink regions are holes in the material. For each imaged hole in the sample support, the total number of black pixels and valid pixels (total area excluding holes and sample support) was summed up, with the clean area in % being calculated as the fraction of black pixels to all valid pixels.

Monolayer area estimation— MAADF-STEM images of entire holes in the sample support (Figure S3a) that visibly contain multilayer areas were analyzed to estimate the amount of exposed monolayer area for each imaged hole. They underwent an image thresholding and segmentation process analogous to the one outlined above. This way, the clean monolayer was separated from contamination and multilayer structures, as well as the sample support and holes in the material (Figure S3b). This resulting binary image was then subjected to a series of four erosion processes, followed by four dilation processes, each with a circular 21×21 px kernel to remove contamination while retaining the general size and shape of (large) multilayer structures (Figure S3c). Then, area opening was performed to remove connected contaminated areas that survived the previous process. The size threshold was varied between 2500 nm^2 and 6000 nm^2 depending on the frame. Finally, a circular mask with a diameter between 900 nm and 1000 nm (depending on the frame) was applied to mask areas containing the sample support (Figure S3d). The monolayer area was then approximated by calculating the number of black pixels divided by the number of non-masked pixels. Figure S3e shows the mask containing multilayer (white) and holes (pink) overlaid on top of the original image.

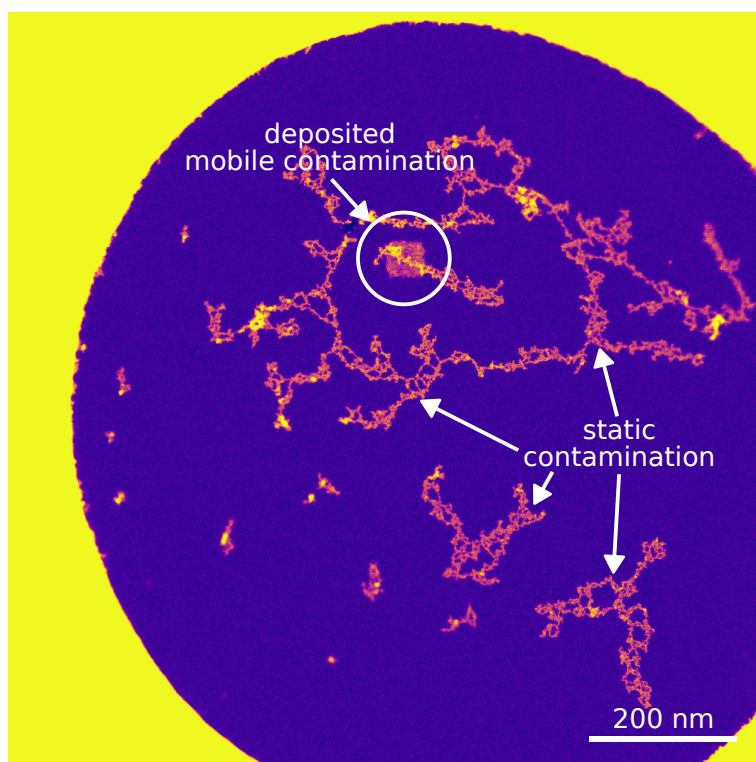
Mobile contamination

While we claim to have achieved large-area atomically clean graphene and h-BN, we cannot completely exclude the presence of hydrocarbon species diffusing on the surface ("mobile contamination"), as there have been reports of their existence even when the sample is kept at 800°C during STEM imaging^[3]. Their presence is difficult to directly image until they stick to the surface via e-beam-induced hydrocarbon deposition, where the hydrocarbon molecules are dissociated by the e-beam and then undergo a cross-linking process until they eventually stick to the surface. However,



Supplementary Figure S3: **Relative multilayer estimation of suspended h-BN.** a) MAADF-STEM image of a hole in the sample support. The darkest contrast is holes, the second darkest contrast is clean monolayer h-BN, and brighter features are multilayer structures and contamination. The bright features in the corners are the sample support. b) Original binary image after the thresholding process. Here, black pixels are clean monolayer regions, and white pixels are contamination, multilayer structures, and the sample support. c) Panel b) after five consecutive erosion and dilation steps, followed by area opening. Here, black pixels mark monolayer regions (regardless of contamination inside them). d) Final segmented image, where black areas are monolayer h-BN, pink areas are holes, white areas are multilayer structures, and the grey region masks the sample support. e) Mask obtained in panel d) overlaid on top of the original image in panel a), where only monolayer regions are not masked.

we did not observe this behavior even during extensive imaging on the same day the bake had been carried out, as can be seen in Supplementary Video 1 and Supplementary Video 2 (4 μ s pixel time, 130 pA beam current, 32x32 nm² nominal FOV, 512x512 px). However, after storage in near-UHV conditions for over three weeks, diffuse hydrocarbon molecules were almost immediately deposited onto the surface, even after only brief e-beam exposure (Figure S4), making it practically impossible to image what had previously been identified as atomically clean graphene. It is possible that, immediately after the heating, the residual heat on the sample and sample holder reduced the adsorption of mobile contamination onto them due to their higher temperature compared to the sample stage, a difference that is equalized after longer storage. It may also be the case that contaminant species inside the near-UHV sample storage atmosphere eventually deposit onto the surface, in addition to the diffusion of surface-bound hydrocarbon molecules on the surfaces inside the sample storage chamber. Nevertheless, given that no e-beam-induced hydrocarbon deposition was observed during the initial data collection, we have high confidence that the potential presence of mobile contamination did not affect the measured clean area.

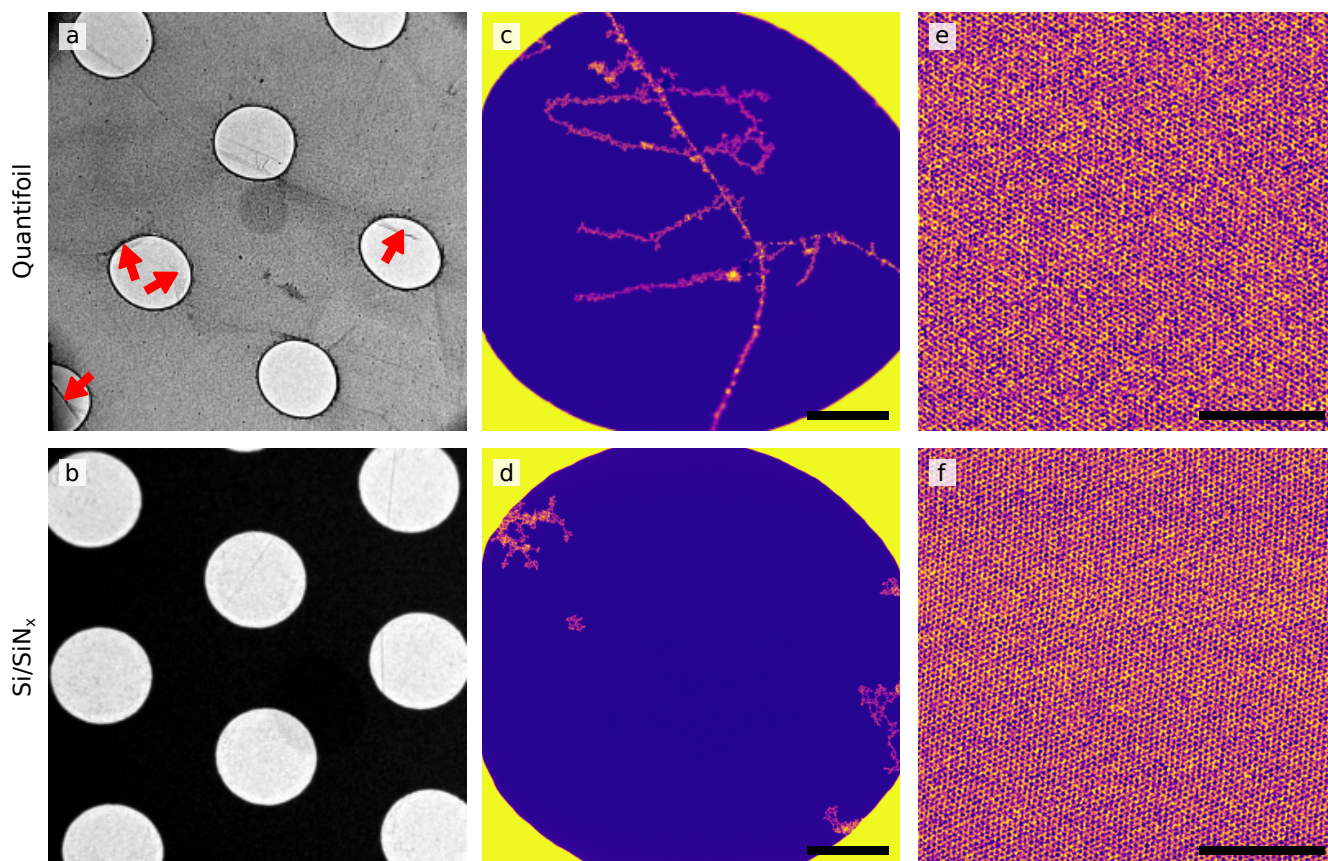


Supplementary Figure S4: **E-beam-induced hydrocarbon deposition on graphene after longer UHV storage.** MAADF-STEM image of clean freestanding graphene (darkest contrast) with (static) dendritic contamination structures (brighter contrast) on its surface, where the visible square (white circle) originates from mobile contamination being pinned down due to e-beam-induced hydrocarbon deposition with the scanning probe.

Sample support damage

At higher annealing temperatures, we observe substantial warping and damage of the structural sample support, likely occurring from the mismatch of the thermal expansion coefficient of the gold bars and amorphous carbon film, in addition to thinning of the already thin (ca. 10 nm) amorphous carbon support membrane. Figure S5a shows the observed compressions of the imaged projections of the holes in the support film, which manifest as elliptic rather than circular appearing holes, originating from thermally-induced stretching of the sample support. This not only causes mechanical strain, creating tears and cracks in the graphene (red arrows in Figure S5a), but also makes it more difficult to get larger areas into focus at once with the scanning probe due to strong height differences within each hole (Figure S5b), in addition to support-induced vibrations which manifest in non-ideal imaging conditions, limiting acquisition of atomically-resolved images. Therefore, another graphene sample prepared via electrochemical delamination was transferred onto

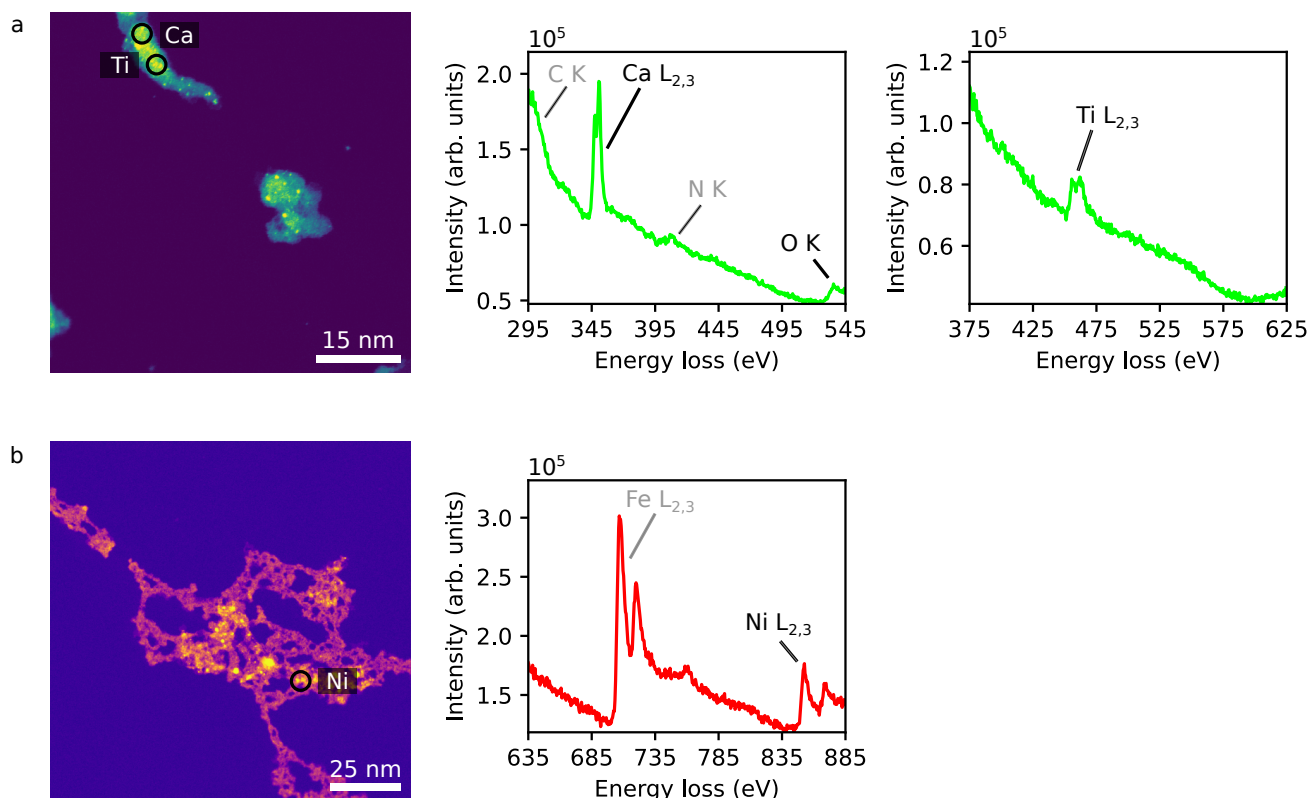
a holey silicon nitride support membrane with a rigid 200 nm membrane thickness and was heated at 450 °C for 2 h in UHV. After annealing at 450 °C, the sample support was still in pristine condition (Figure S5c), mitigating support-induced corrugations of graphene (Figure S5d) and thus also minimizing strain-induced damage to the material. This sample exhibited a similar level of cleanliness as the one on the holey carbon support film that had also been annealed at 450 °C, with a measured average clean area above 95% (Figure 1a, main text, purple dots), slightly higher than the 90% measured from the other sample support. However, we attribute this minimal difference to local differences from the source material and transfer, in addition to contamination overestimation arising from unfocused features caused by the earlier-mentioned height variations in the other samples, rather than due to a different thermal response of the Si/SiN_x compared to the holey amorphous carbon support.



Supplementary Figure S5: **Differences in thermal response of the sample support.** Bright field Ronchigram image of graphene a) on a Quantifoil (QF) holey carbon support film and b) on a perforated Si/SiN_x support after annealing at 450 °C for 3 h. Nominal hole diameters 1 µm. The red arrows in a) point towards damage in the graphene due to sample support warping. MAADF-STEM images showing a typical hole containing clean suspended graphene c) on QF and d) on Si/SiN_x, with higher magnification MAADF-STEM images in e) and f) showing large areas of pristine clean graphene on QF, and Si/SiN_x, respectively. Scale bars: c, d) 200 nm, e, f) 5 nm.

Other trace contaminants

Among the ubiquitous hydrocarbon contamination, as well as the Cu and Fe nanoclusters discussed in the main text, we could also identify other contaminants (Figure S6), namely oxygen, calcium, titanium, and nickel, though rarely. Detecting oxygen was challenging, as we found it not only not to be abundant, particularly after the annealing step, but also due to its decreasing signal strength with prolonged electron beam exposure^[4] during spectrum acquisition, which would be favorable to obtain a better signal-to-noise ratio. However, we could identify it alongside calcium on one of our samples (h-BN annealed at 550 °C), with Ca likely originating from impure deionized water used during the sample transfer process. The concurrent presence of Ca, O, and C suggests calcium oxide or calcium carbonate as the



Supplementary Figure S6: **Identified trace contaminants.** a) Ca L_{2,3} (and O K) and Ti L_{2,3} EEL spectra (not background-subtracted) acquired on contaminated sites (marked in the accompanying MAADF-STEM image) on h-BN after annealing at 550 °C. b) Ni L_{2,3} spectrum (not background-subtracted) acquired within metallic contamination (marked in the accompanying MAADF-STEM image) on graphene after annealing at 450 °C. Core loss edges of other contaminant species (C, Fe) and N from the material are also visible.

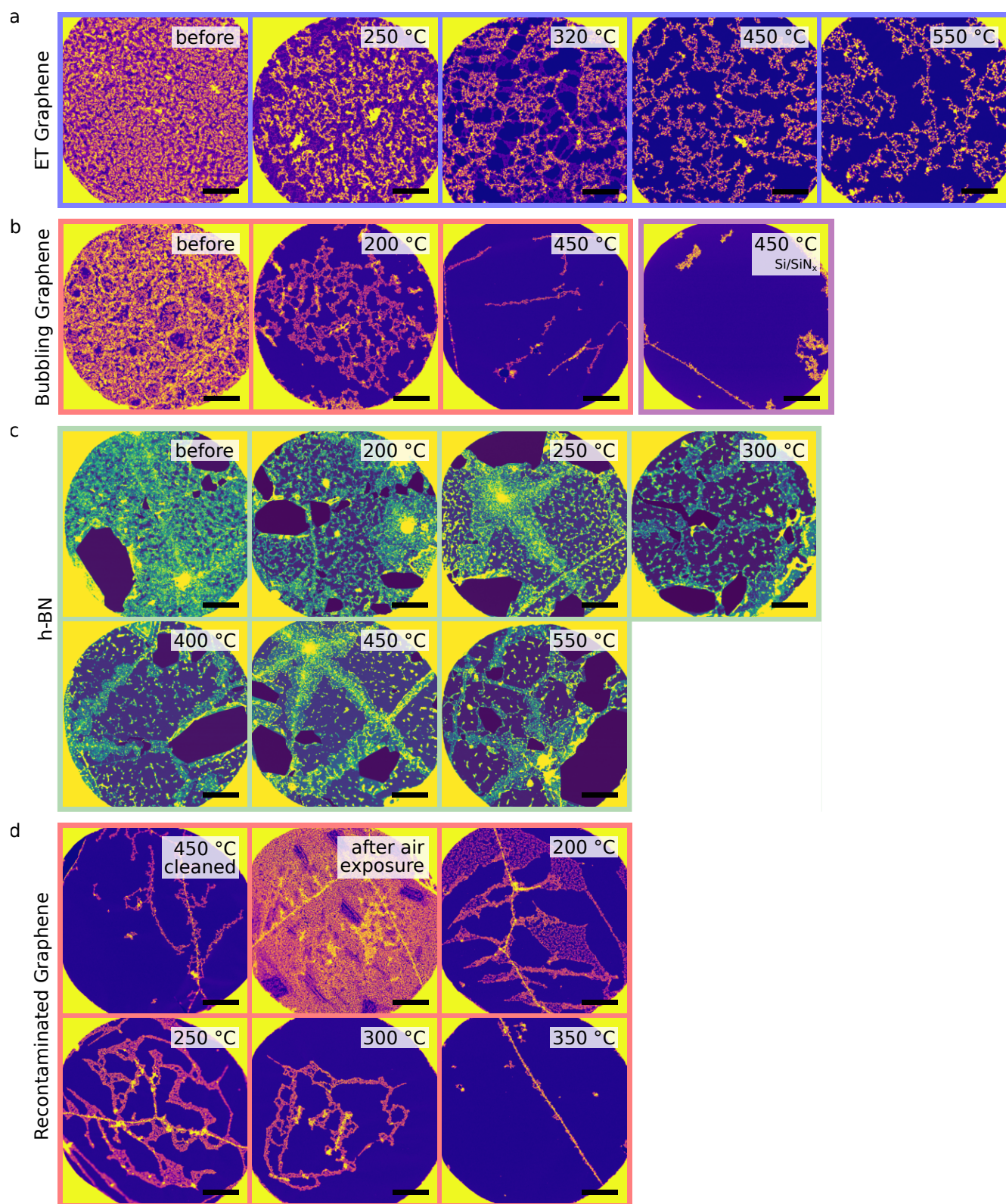
contaminant. We could also identify titanium on some of our samples, in particular ones that have been stored in UHV for longer, likely originating from Ti sputtering from the ion pumps in the vacuum system. Nickel could also be found on one of our graphene samples (annealed at 450 °C) alongside a Fe nanocluster, which could originate from any of the stainless steel parts of the vacuum system, or could have evaporated from the K-type (Ni-Cr/Ni-Al) thermocouple inside the UHV heating chamber during the annealing procedure. If Ni had indeed evaporated from the thermocouple, one would also expect Cr deposition on the sample surface. However, it was not detected on any of the samples analyzed by EELS, although its presence cannot be ruled out without conducting a more thorough investigation.

UHV heating chamber design

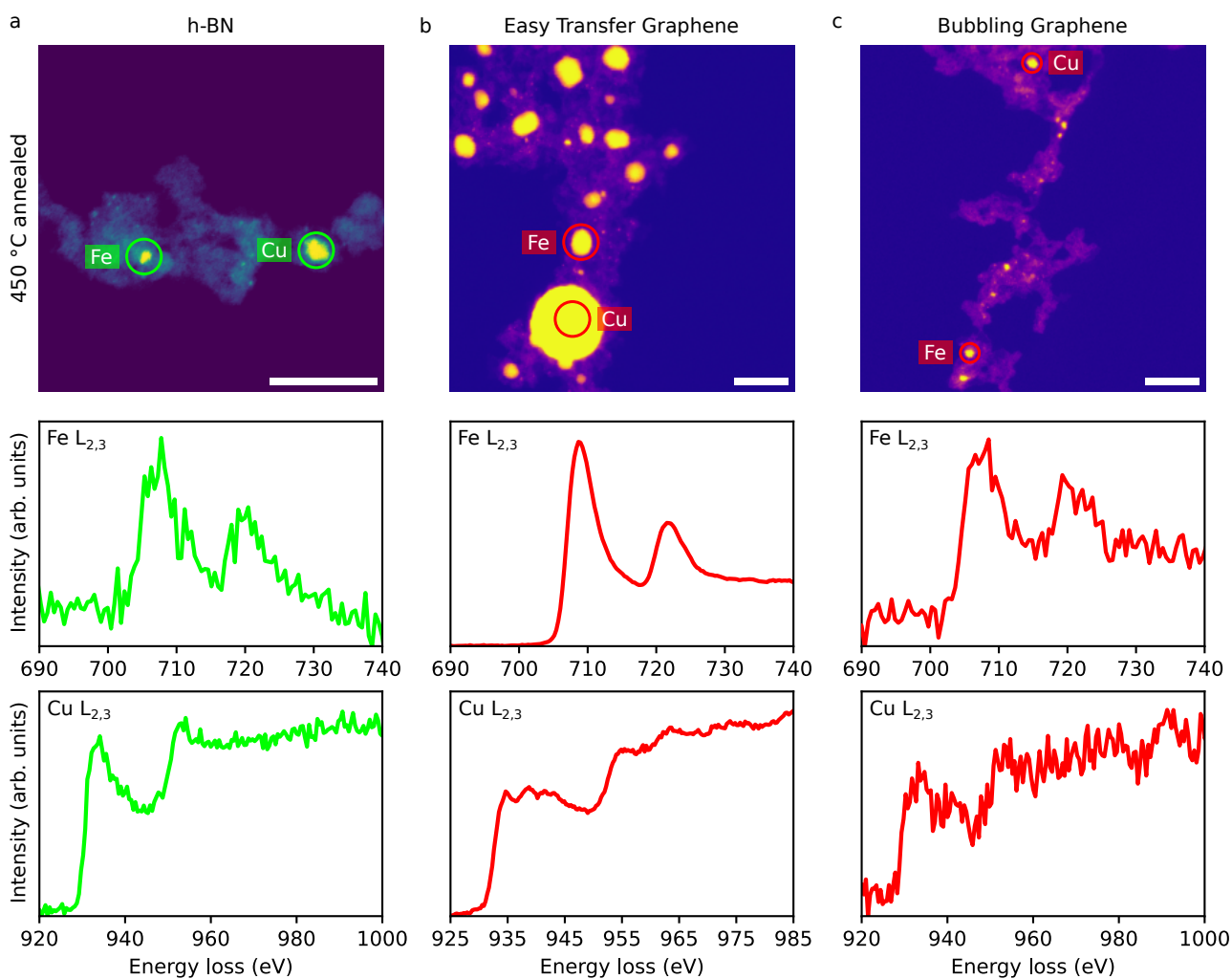
The UHV heating chamber consists of a custom 3D-printed alumina furnace (Figure S15) that accommodates the titanium sample holder, as well as a 0.5 mm thin tungsten filament resting in a 2 mm thick cavity responsible for the resistive heating process. The filament is placed just out of line of sight of the sample to avoid locally high temperatures and allow a more accurate temperature measurement using an ungrounded Inconel 600-sheathed and mineral-insulated K-type thermocouple, which is positioned approximately 1 mm away from the sample and is in physical contact with the sample holder. The oven is encompassed in a cylindrical stainless steel frame (Figure S16) with holes on one of the flat sides of the cylinder (Figure S17) to attach the control electronics and temperature probe, and a sample holder entry on the opposing flat side of the cylinder (Figure S18). The whole assembly is mounted to a zero-length reducing flange at the back of the chamber through stainless steel rods (Figure S19), and is integrated within the interconnected UHV system CANVAS at the University of Vienna^[5].

References

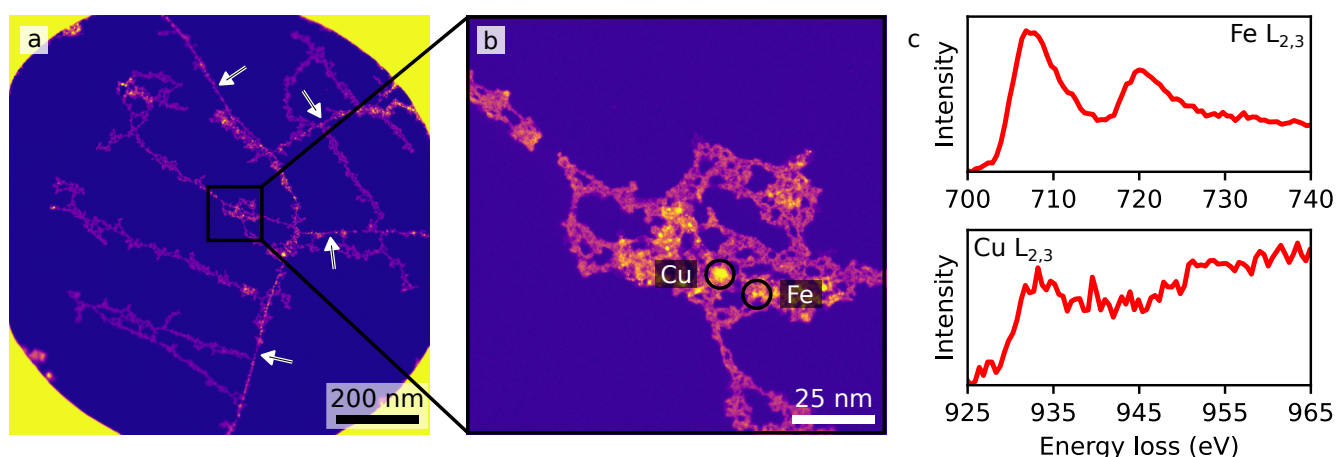
- [1] C. Speckmann, A. Angeletti, L. Kývala, D. Lamprecht, F. Herterich, C. Mangler, L. Filipovic, C. Dellago, C. Franchini, and J. Kotakoski. Electron-Beam-Induced Adatom-Vacancy-Complexes in Mono- and Bilayer Phosphorene. *Advanced Materials Interfaces* **12** (2025), 2400784. DOI: 10.1002/admi.202400784.
- [2] T. Susi, T. P. Hardcastle, H. Hofsäss, A. Mittelberger, T. J. Pennycook, C. Mangler, R. Drummond-Brydson, A. J. Scott, J. C. Meyer, and J. Kotakoski. Single-atom spectroscopy of phosphorus dopants implanted into graphene. *2D Materials* **4** (2017), 021013. DOI: 10.1088/2053-1583/aa5e78.
- [3] O. Dyck, A. Okmi, K. Xiao, S. Lei, A. R. Lupini, and S. Jesse. Your Clean Graphene is Still Not Clean. *Advanced Materials Interfaces* **12** (2025), 2400598. DOI: 10.1002/admi.202400598.
- [4] G. T. Leuthner, S. Hummel, C. Mangler, T. J. Pennycook, T. Susi, J. C. Meyer, and J. Kotakoski. Scanning transmission electron microscopy under controlled low-pressure atmospheres. *Ultramicroscopy* **203** (2019), 76–81. DOI: 10.1016/j.ultramic.2019.02.002.
- [5] C. Mangler, J. Meyer, A. Mittelberger, K. Mustonen, T. Susi, and J. Kotakoski. A Materials Scientist's CANVAS: A System for Controlled Alteration of Nanomaterials in Vacuum Down to the Atomic Scale. *Microscopy and Microanalysis* **28** (2022), 2940–2942. DOI: 10.1017/S1431927622011023.



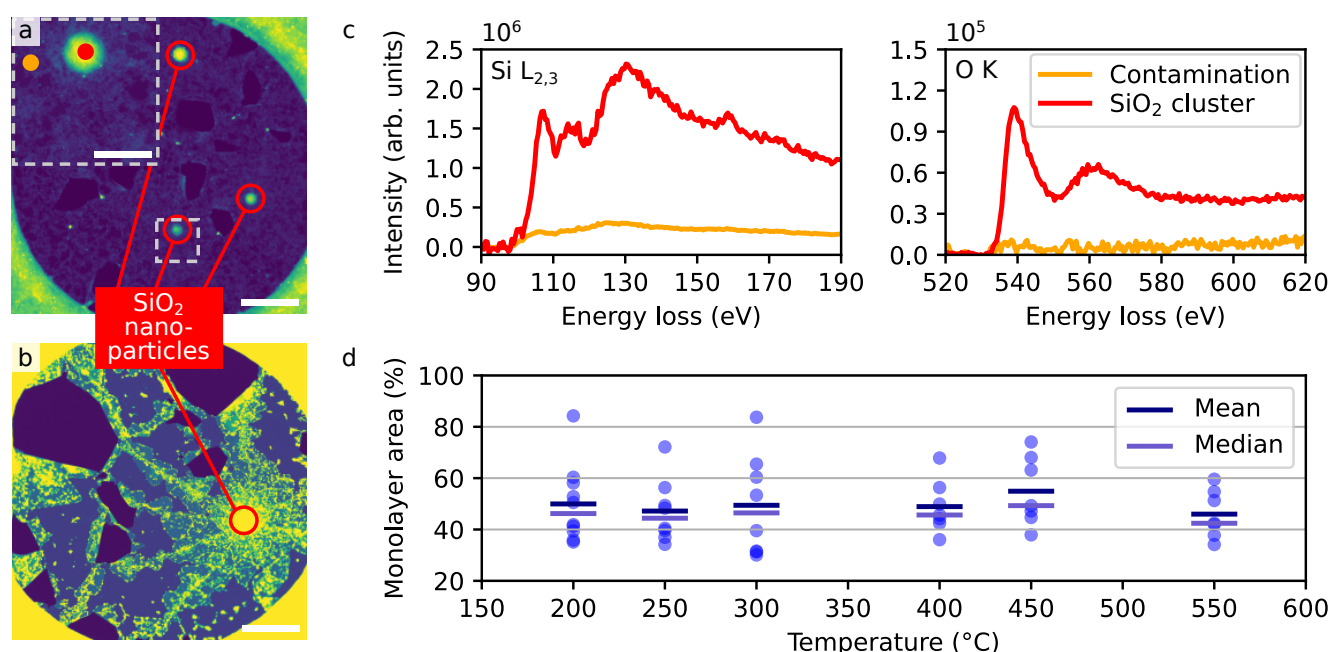
Supplementary Figure S7: **MAADF-STEM images of non-cropped frames used for temperature comparison.** Original (non-cropped) images of the cropped MAADF-STEM images shown in a,b) Figure 1, c) Figure 3, and d) Figure 4 (main text). Scale bars: 200 nm.



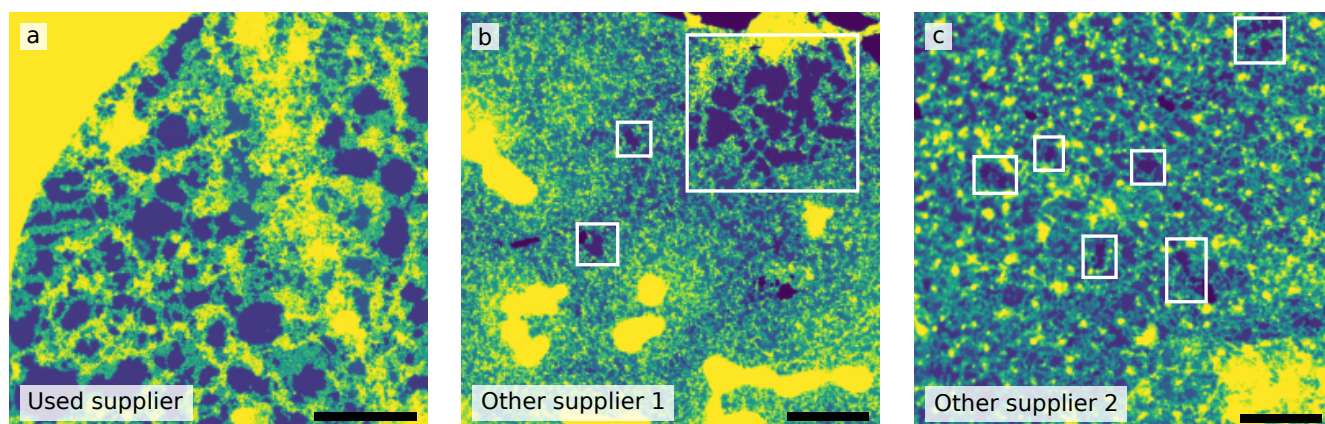
Supplementary Figure S8: **EELS of metal contaminants.** Fe $L_{2,3}$ and Cu $L_{2,3}$ EEL spectra and accompanying MAADF-STEM (HAADF-STEM in panel a) images acquired on metallic contamination (colored circles) of a) h-BN, b) Easy Transfer Graphene, and c) graphene transferred via electrochemical delamination after annealing at 450 °C for 3 h. Scale bars: 10 nm.



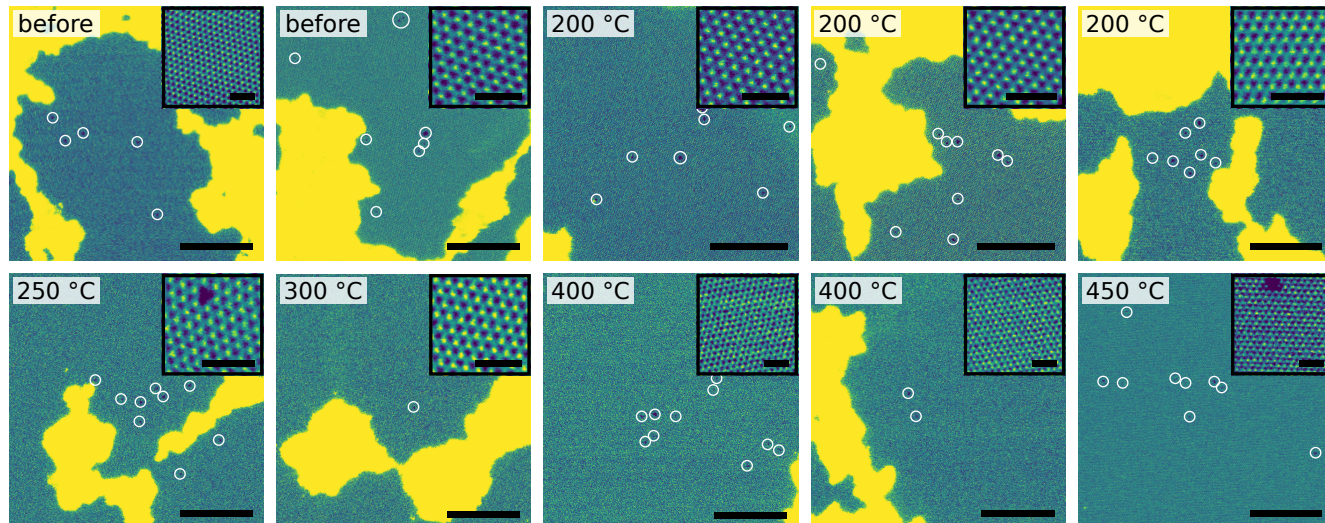
Supplementary Figure S9: **Dendritic contamination structures emerging from ensembles of metal nanoclusters.** a) MAADF-STEM image of an example hole in the sample support with multiple grain boundaries (marked by white arrows) and a large amount of dendritic contamination structures. b) Higher magnification of the boxed area in a) showing an ensemble of Cu and Fe nanoclusters. c) Fe L_{2,3} and Cu L_{2,3} EEL spectra acquired inside the circles highlighted in panel b).



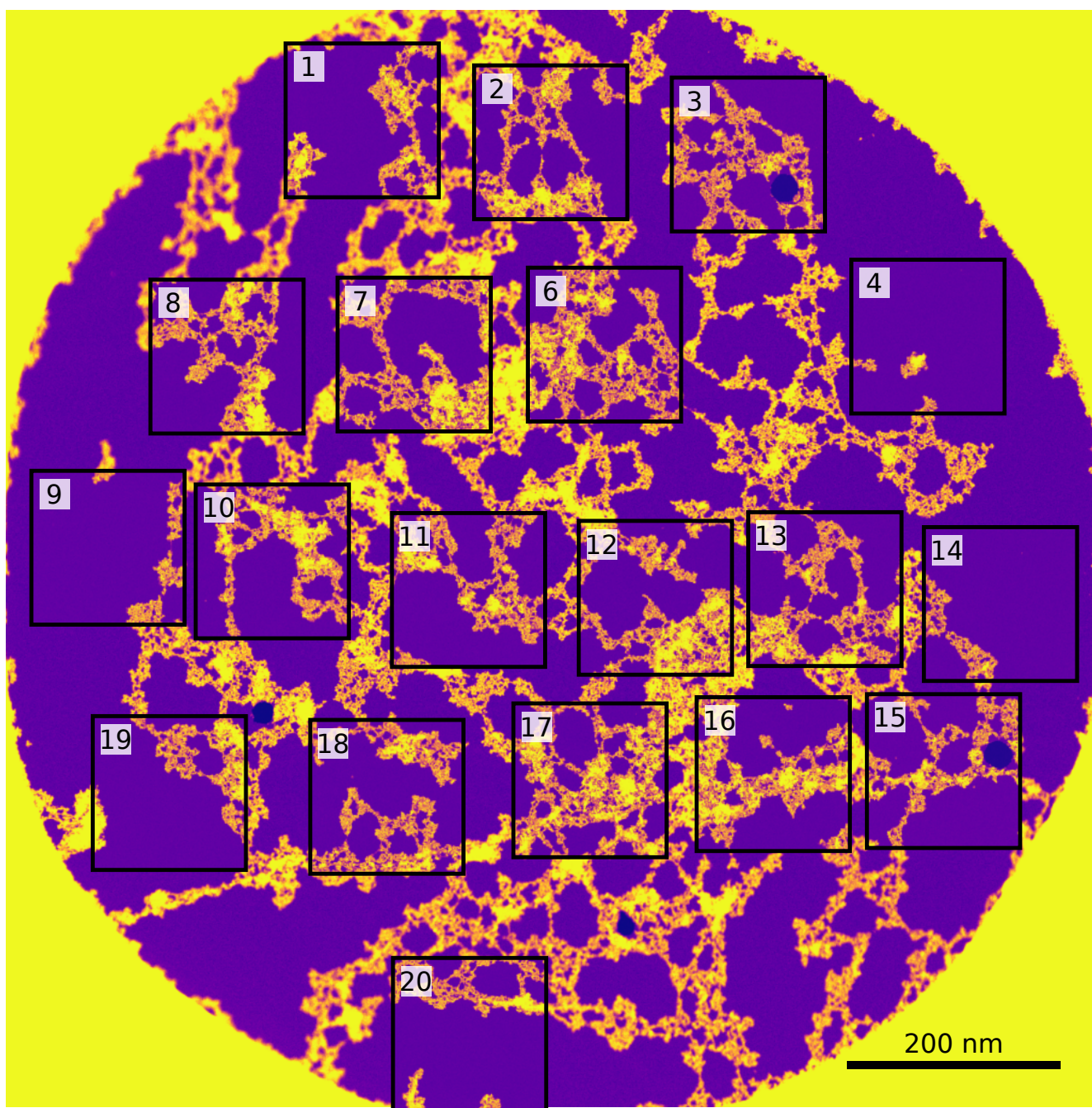
Supplementary Figure S10: **SiO₂ nanoclusters on h-BN.** MAADF-STEM images of SiO₂ nanoparticles (marked with red circles) on a) dirty and b) cleaned h-BN. The inset in a) shows a selected particle at higher magnification. A different contrast enhancement in panel a) was chosen to highlight the morphologies of the spherical SiO₂ nanoparticles. The colored dots represent the positions where EEL spectra were acquired. c) Si L_{2,3} and O K EEL spectra acquired on hydrocarbon contamination (orange) and a SiO₂ nanoparticle (red). d) Estimated h-BN monolayer coverage from different samples annealed at different temperatures. Each dot represents a different hole in the sample support. Scale bars: 200 nm (inset: 25 nm).



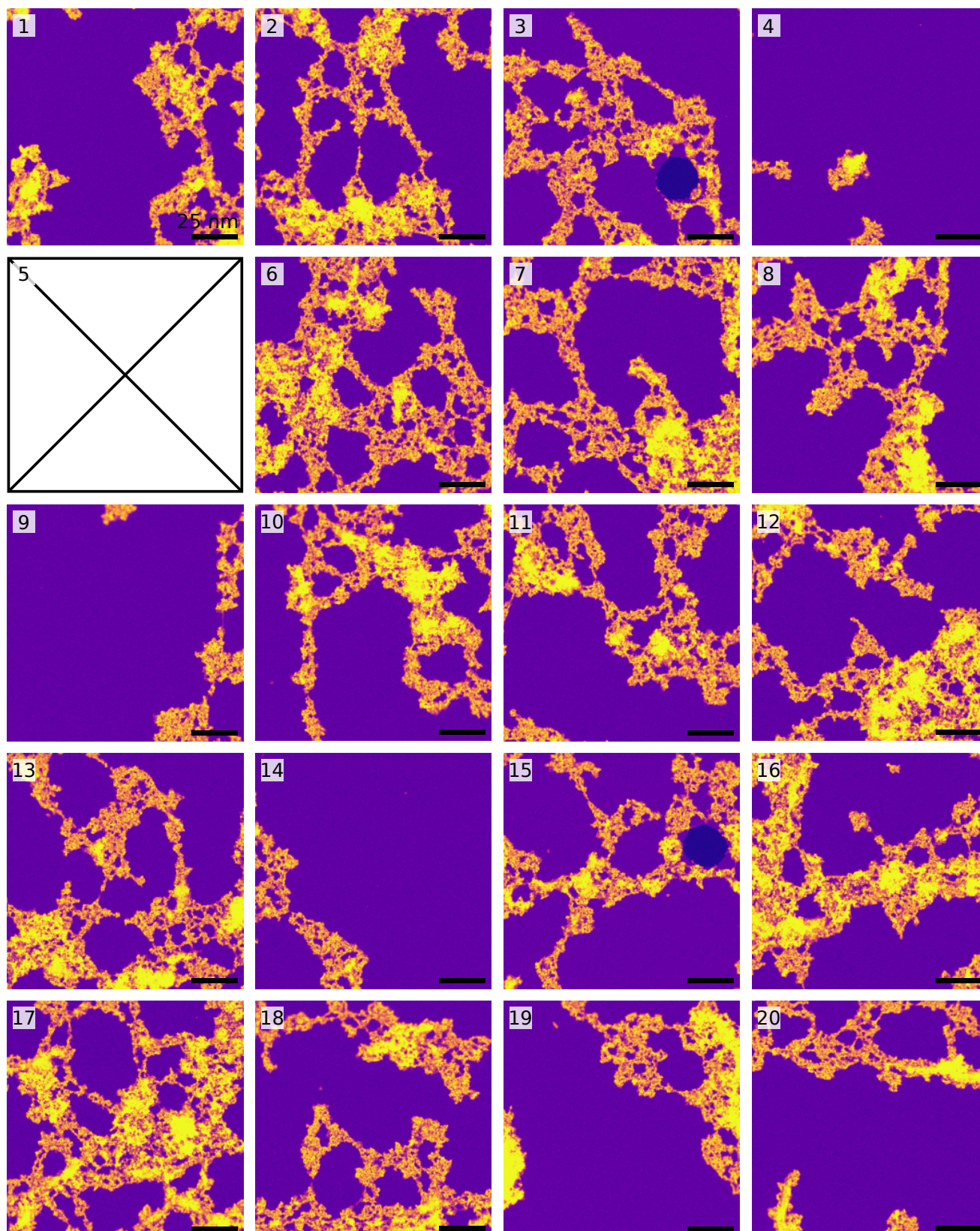
Supplementary Figure S11: **MAADF-STEM images comparing the monolayer coverage from different suppliers.** a) Free-standing h-BN from the supplier used in this work. All areas with the darkest contrast are monolayer h-BN. Brighter features are bilayer regions, contamination, and the sample support (top left corner). The materials supplied by b) other supplier 1 and c) other supplier 2 exhibit a much lower amount of monolayer h-BN, where areas of notable sizes are highlighted with white rectangles. Scale bars: 100 nm.



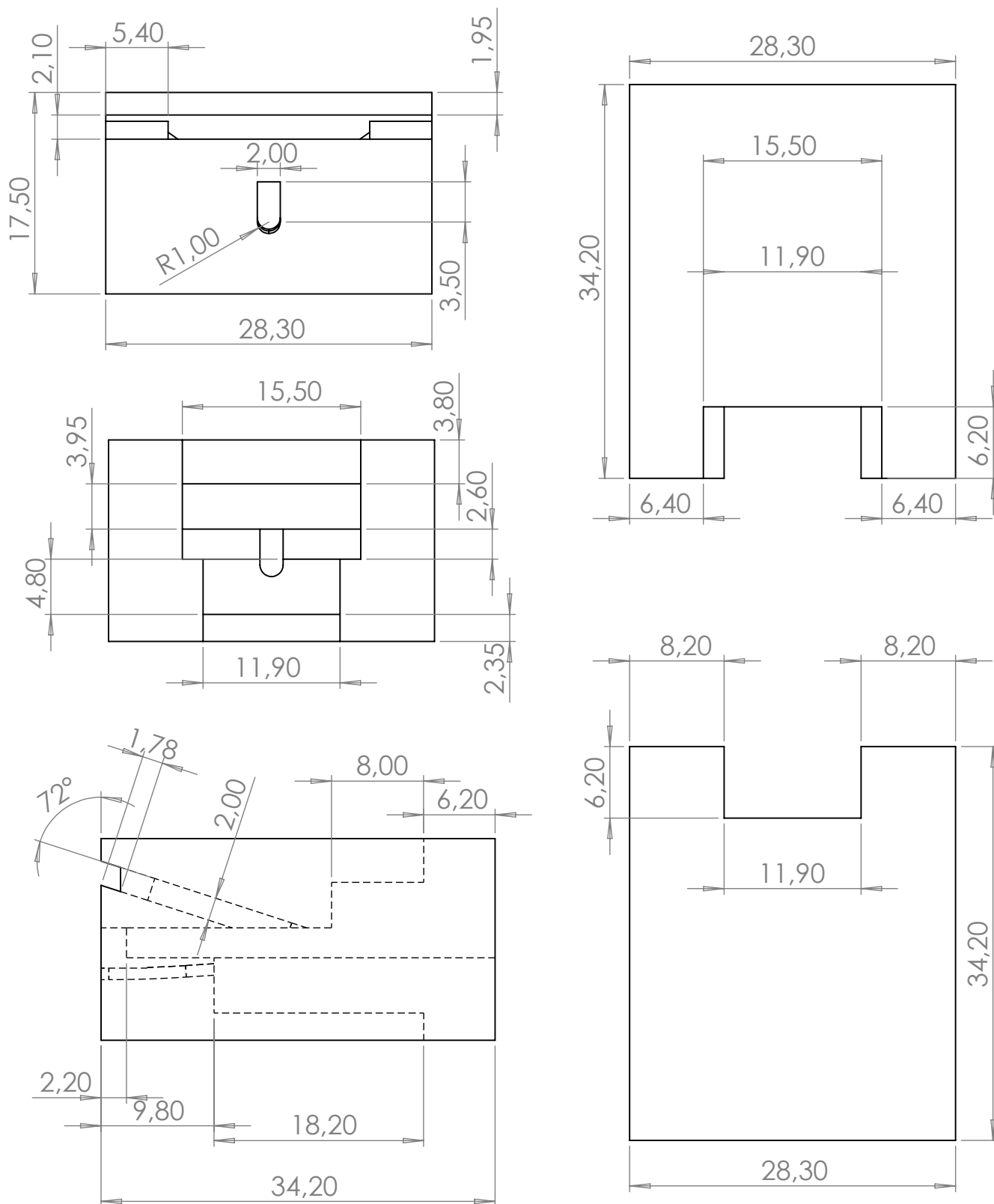
Supplementary Figure S12: **Point defects in h-BN.** Examples of observed point defects in h-BN after annealing at different temperatures. Regions where vacancies could be unambiguously identified are marked with white circles. Images shown in the insets were taken towards the center of the corresponding frames. The higher defect density towards the center of each frame is due to prior e-beam exposure for the acquisition of the images in the insets. Scale bars: 10 nm (insets: 1 nm).



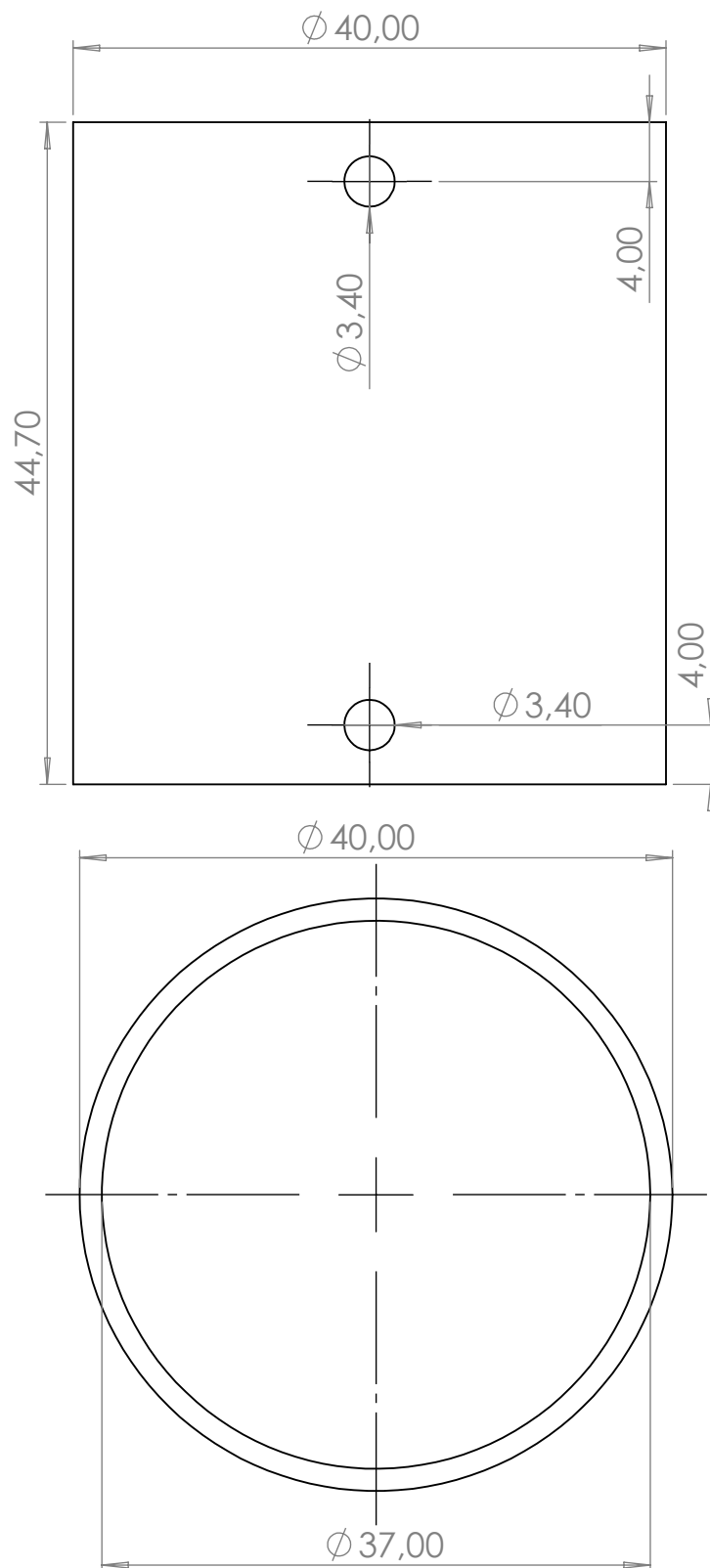
Supplementary Figure S13: **Depiction of the image acquisition process within one example hole in the sample support.** MAADF-STEM images of monolayer graphene showing the positions of acquired frames within a hole in the sample support. The darkest contrast is holes in the material, corresponding to vacuum intensity (see, for example, frames 3 and 15), the second darkest contrast is clean monolayer graphene. Individually acquired frames (nominal FOV $128 \times 128 \text{ nm}^2$) are overlaid on top of an overview image of the entire hole in the background. The numbers in the top left corners of the insets indicate the respective frames in the hole, listed in the order of acquisition. Here, frame 5 was removed due to significant overlap with frame 4.



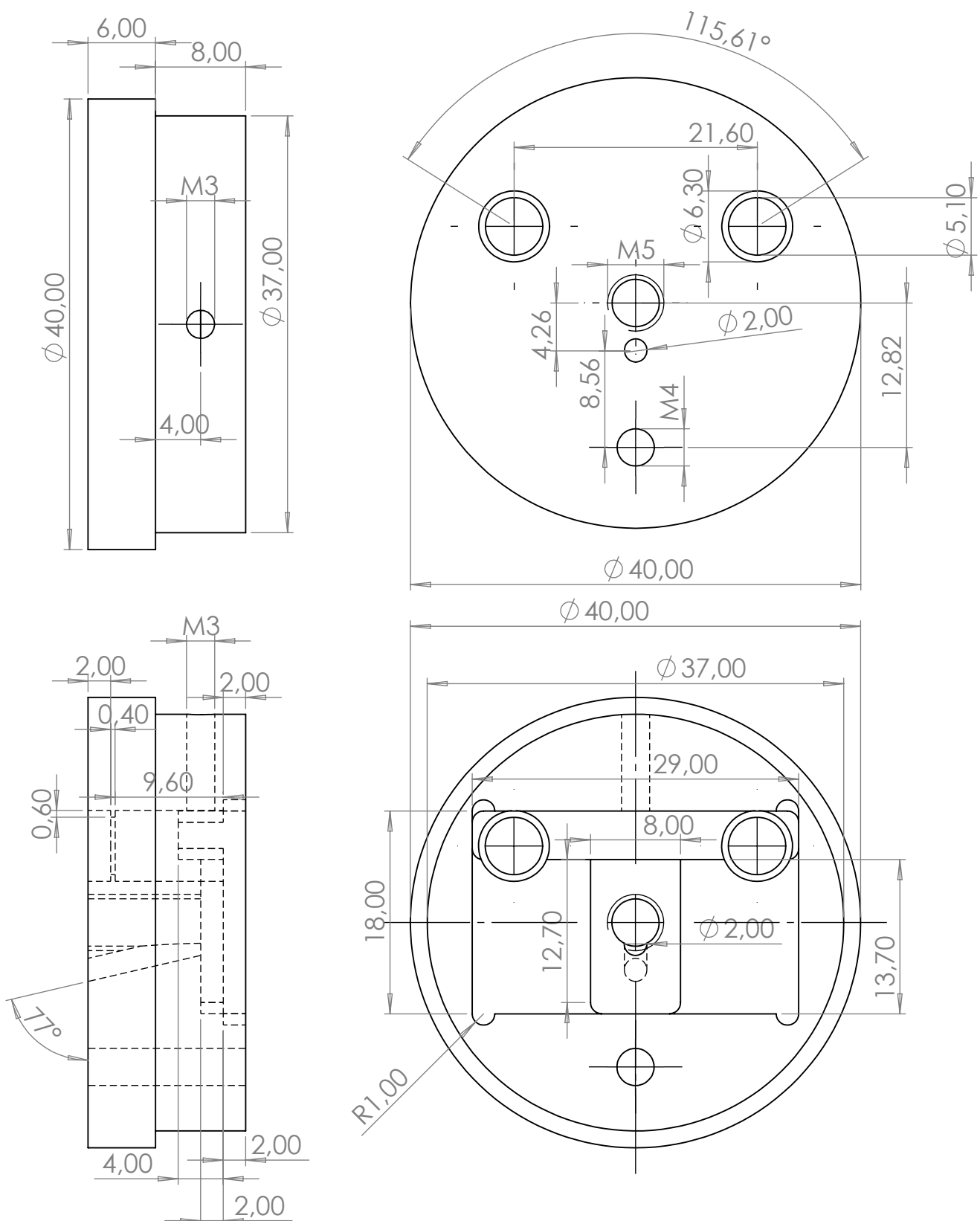
Supplementary Figure S14: **MAADF-STEM images of all frames of one example hole for graphene (see Figure S13).** The numbers in the top left corners of the other images shown here correspond to the respective frames acquired in the hole. In all images, the darkest contrast is that of clean monolayer graphene, except for frames 3 and 15, where the darkest contrast corresponds to holes in the material and represents the vacuum intensity. For the calculation of the relative clean area, the number of pixels of all frames acquired within one hole is summed up (see Digital image processing, Supporting Information). Here, 65% of the total covered area is clean monolayer graphene. Here, frame 5 was removed due to significant overlap with frame 4.



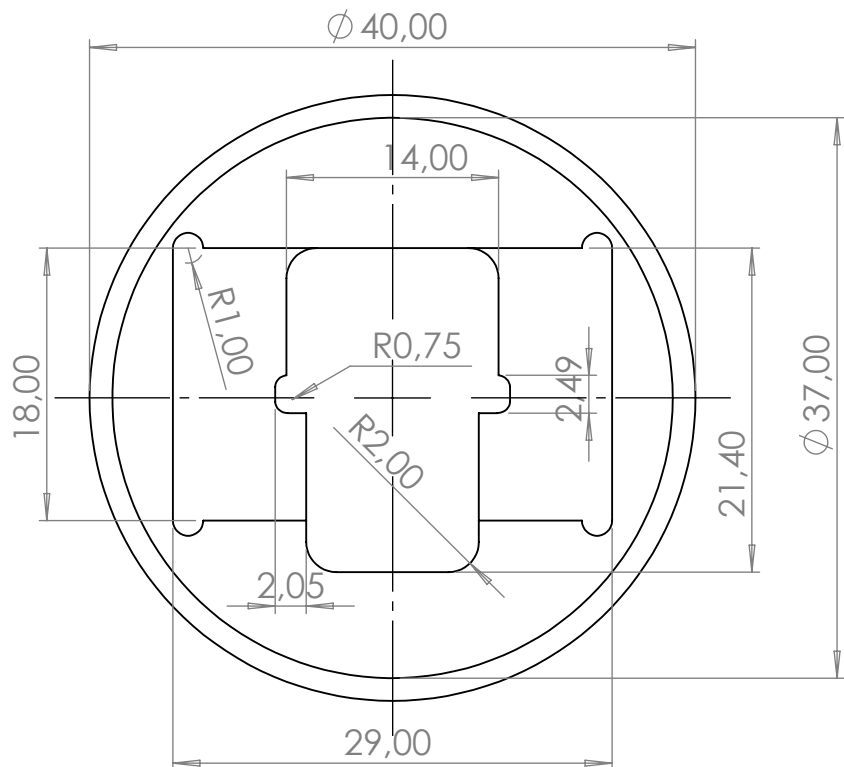
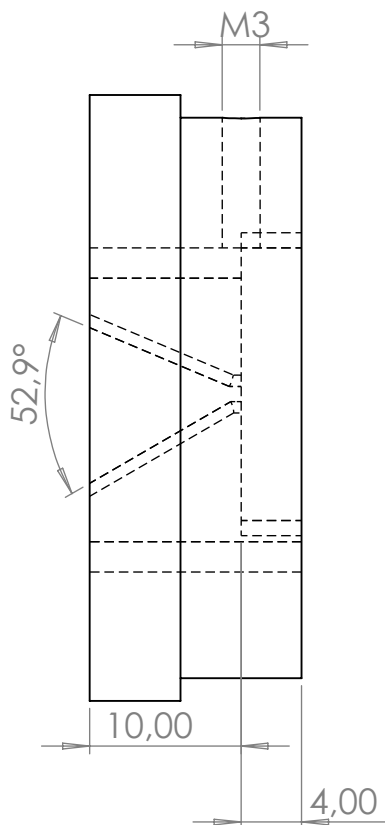
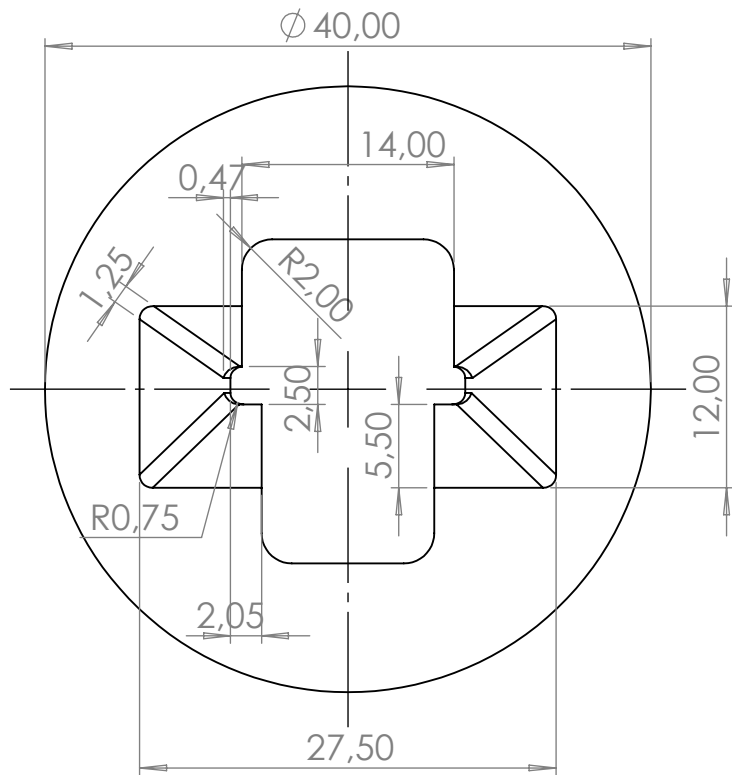
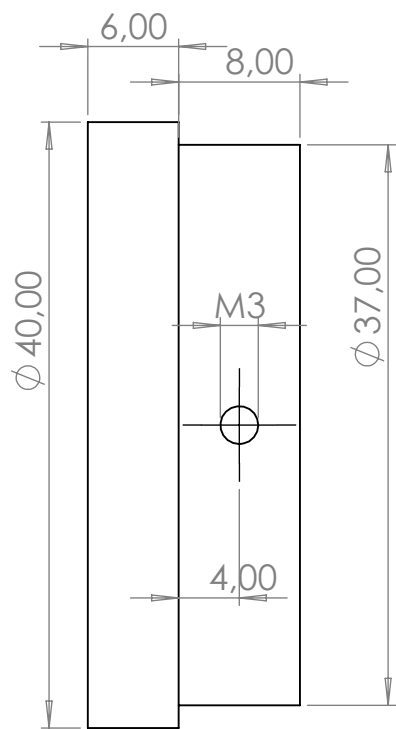
Supplementary Figure S15: **Construction plan for the 3D-printed alumina furnace.** Back, front, side, top, and bottom view orientations of the alumina furnace, with measurements of distances, angles, and hole radii are displayed. All lengths in mm.



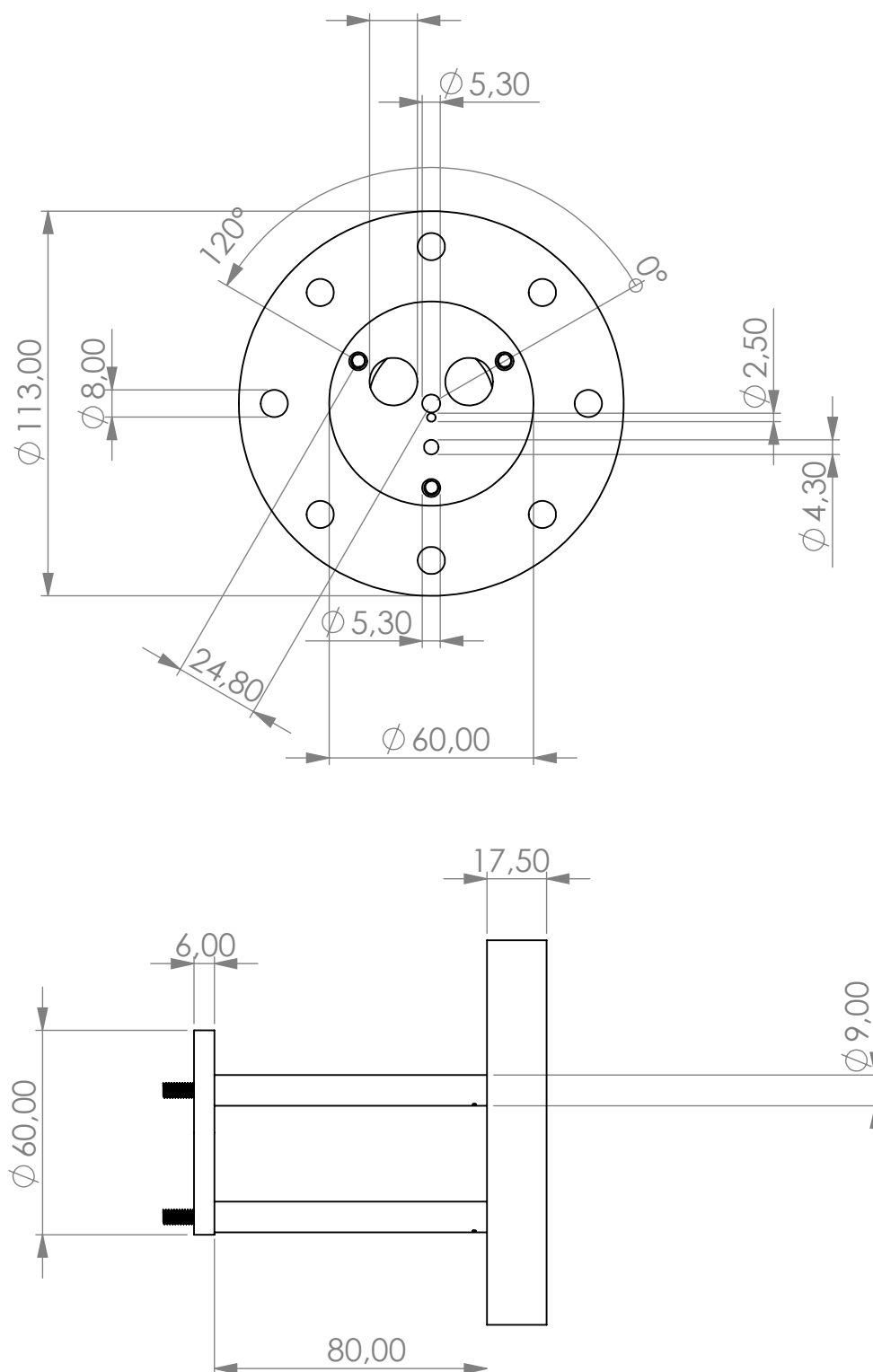
Supplementary Figure S16: **Construction plan for the cylindrical stainless steel frame of the oven.** Top and front view orientations of the alumina furnace, with measurements of distances and hole radii are displayed. All lengths in mm.



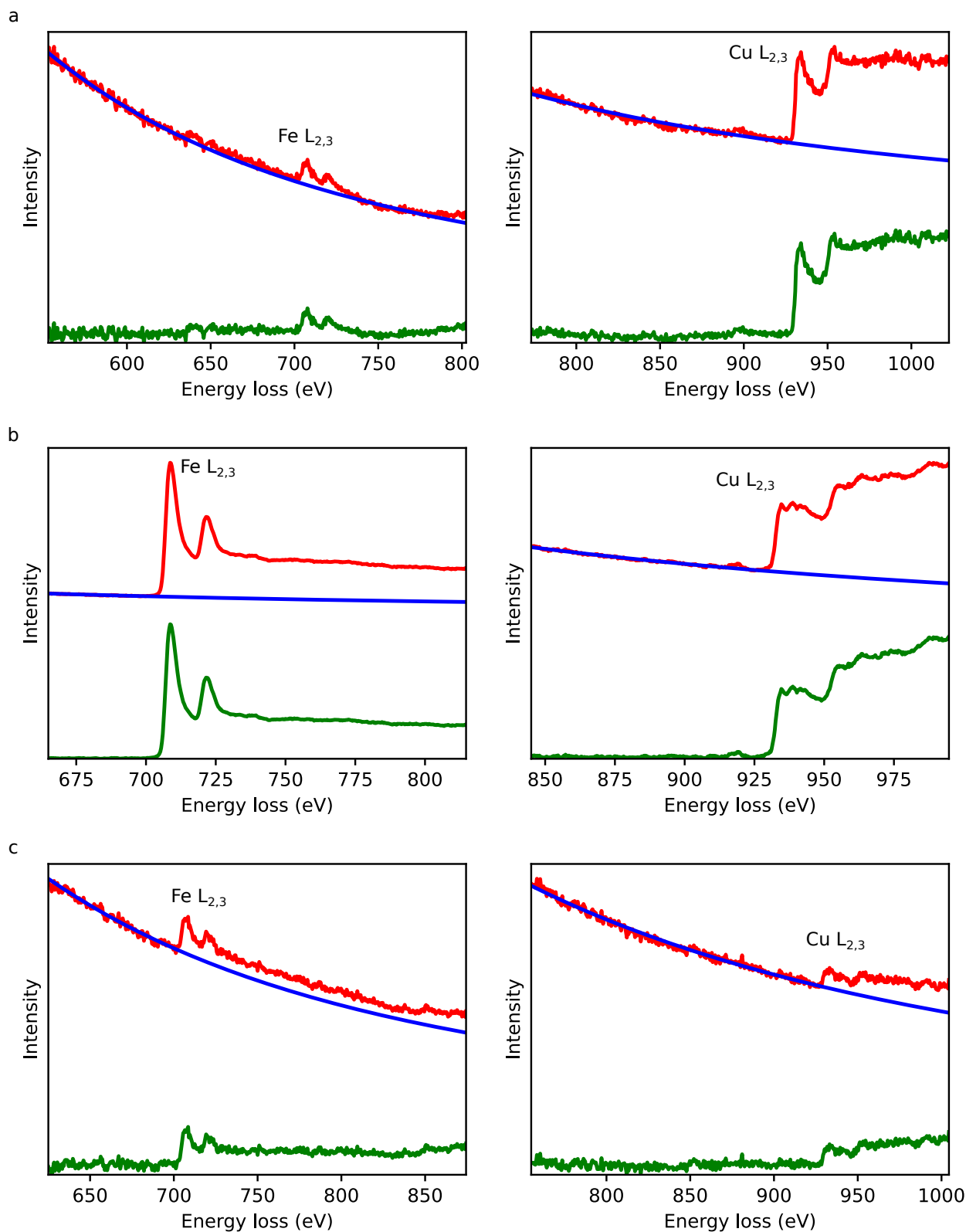
Supplementary Figure S17: **Construction plan for the backside of the oven.** Top, side, front, and back view orientations of the backside of the oven frame, with measurements of distances, angles, and hole diameter, are displayed. ISO metric screw threads (M3, M4, M5) are used. All lengths in mm.



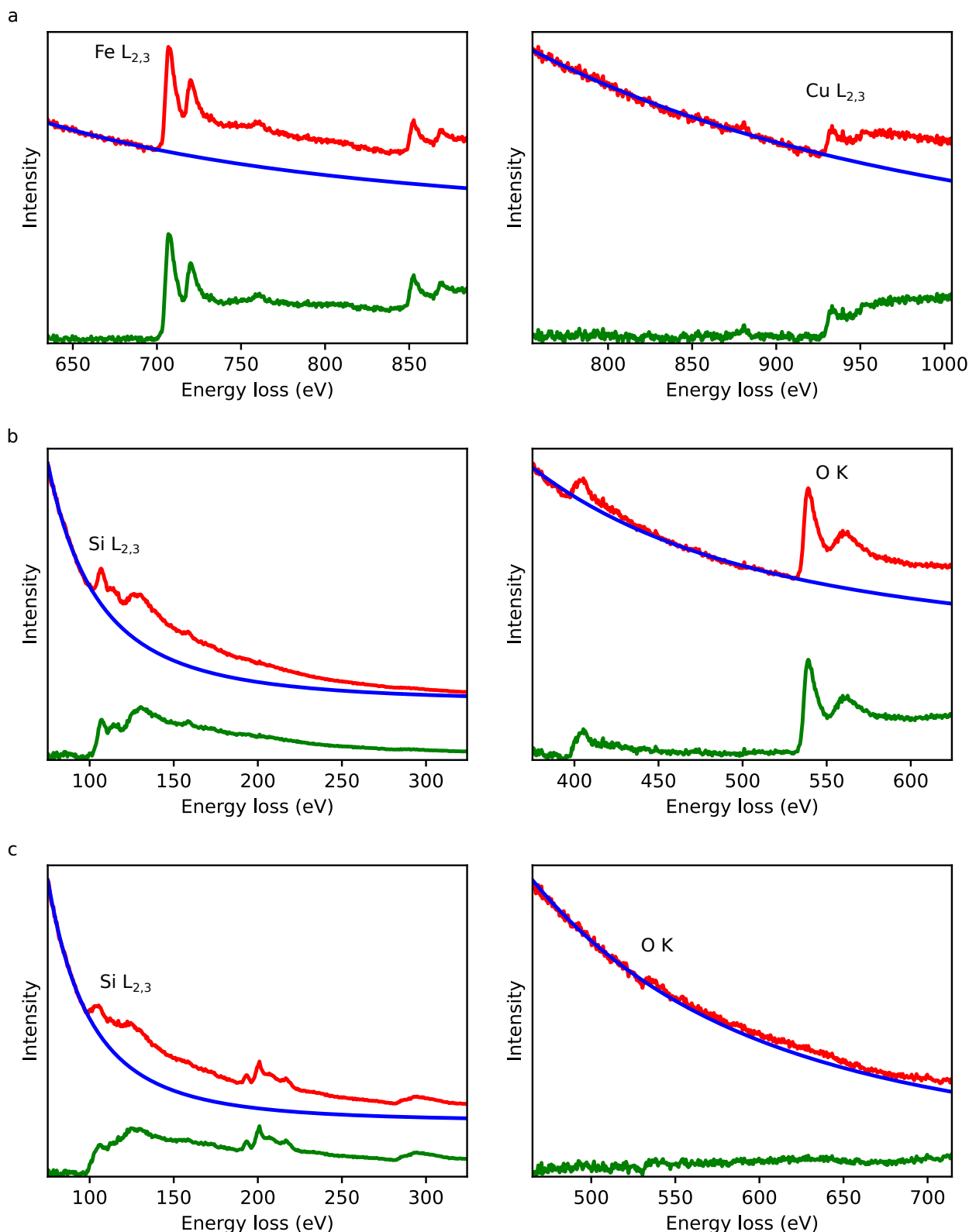
Supplementary Figure S18: **Construction plan for the frontside of the oven.** Top, side, front, and back view orientations of the backside of the oven frame, with measurements of distances, radii, fillet radii, and angles, are displayed. ISO metric screw threads (M3) are used. All lengths in mm.



Supplementary Figure S19: **Construction plan for the UHV heating chamber fixture assembly.** Front and side view orientations of the backside of the oven frame, with measurements of distances, angles, and hole radii, are displayed. All lengths in mm.



Supplementary Figure S20: **Original EEL spectra including background subtraction.** Original Fe $L_{2,3}$ and Cu $L_{2,3}$ spectra (red) with added vertical offset, power law background subtraction function (blue), and resulting background-subtracted spectra (green) acquired on iron and copper clusters a) on h-BN (Figure S8a), b) on Easy Transfer Graphene (Figure S8b), c) on graphene transferred via electrochemical delamination (Figure S8c) after annealing at 450 °C for 3 h.



Supplementary Figure S21: **Original EEL spectra including background subtraction.** Original spectra (red) with added vertical offset, power law background subtraction function (blue), and resulting background-subtracted spectra (green) acquired a) on iron and copper clusters within agglomerations of metal clusters on graphene transferred via electrochemical delamination after annealing at 450°C for 3 h (Figure 2), b) on a SiO₂ nanocluster on h-BN before annealing, c) on hydrocarbon contamination next to a SiO₂ nanocluster on h-BN before annealing (Figure S10c). Clearly visible are also the a) Ni L_{2,3}, b) N K, and c) B K, and C K core loss edges.